RESEARCH ARTICLE

Key Points:
- Laboratory loading test on prismatic Carrara marble specimens containing single preexisting flaw has been conducted
- A method for multiscale interpretation of fracture processes has been proposed
- Real-time continuous comparison between acoustic emission moment tensor inversion and optical observation has been conducted

A Method for Multiscale Interpretation of Fracture Processes in Carrara Marble Specimen Containing a Single Flaw Under Uniaxial Compression

Louis Ngai Yuen Wong[1,2] [ID] **and Qiquan Xiong[3]** [ID]

[1]Department of Earth Sciences, The University of Hong Kong, Pok Fu Lam, Hong Kong, [2]Faculty of Engineering, China University of Geosciences, Wuhan, China, [3]School of Civil and Environmental Engineering, Nanyang Technological University, Singapore

Abstract This paper presents a method for continuous multiscale observation of uniaxial compressive tests of Carrara marble specimens containing a single preexisting artificially created flaw. The experiments aim at analyzing the associated mesoscale-macroscale phenomena in the fracture process of the specimens. In the macroscale, the crack types are observed and characterized by optical observation using a camcorder and a high-speed camera. In the mesoscale, the crack types are analyzed and characterized by the moment tensor inversion of acoustic emission. For the experimental investigation on the fracture process on specimens containing a single preexisting flaw, it is the first time quantitative and continuous interpretation and comparison of the mesoscale-macroscale fracture process have become available. The present findings provide substantial improvement on our understanding of the mesoscale-macroscale fracture process in rock specimens containing a single preexisting flaw. In addition, the experimental results provide insightful information about the laboratory scale fault extension and propagation and laboratory scale acoustic emission moment-frequency distribution. The findings are helpful for establishing the link between the laboratory scale tests and the tectonic scale seismic activities.

1. Introduction

The experimental tests on rock and rock-like specimens containing a single preexisting flaw have been extensively conducted by different researchers. However, its fracture process has not yet been fully understood. Lajtai (1974) conducted uniaxial compressive tests on modeled Plaster of Paris specimens containing a single preexisting flaw. In his study, specimens containing a flaw at different inclination angles (from 0 to 90° in 5° intervals) and lengths (1.3, 3.8, and 7.6 mm) were examined. Based on his observation, the sequence of fracture process was (a) tensile fracture, (b) normal shear fracture, (c) expansion into a shear zone through subsequent normal shear and perhaps tensile fractures, and (d) inclined shear fractures in the granulated cohesionless zone. Ingraffea and Heuze (1980) conducted uniaxial compressive tests on limestone specimens containing a single preexisting flaw (flaw length × flaw aperture = 10 mm × 0.2 mm). Petit and Barquins (1988) conducted uniaxial/biaxial compressive tests in low- and high-porosity sandstone specimens containing a single preexisting flaw. They observed cataclastic deformation in the shear zone of mode II macroscale propagation. This observation suggested that "mode II (fracture) cannot exist as an elementary (primary) fracture mechanism (in rock) but can only be a macroscopic fracture phenomenon which must necessarily involve tensile (mode I) micro-crack formation." In their definition, modes I and II were interchangeable with the terms of tensile and shear (cracking/propagation), respectively. Huang et al. (1990) conducted uniaxial compressive tests on Fangshan marble specimens containing a single preexisting flaw (20 mm × 0.1 mm). In their tests, the displacement field contours were used to identify the cracking types in the fracture process. Li et al. (2005) conducted uniaxial compressive tests on Huangshi marble specimens containing a single preexisting flaw (0.5–1 mm aperture with 6-mm diameter center hole; the length was not given). Wong and Einstein (2009a) conducted uniaxial compressive tests on modeled gypsum and Carrara marble specimens containing a single flaw. In their research, a systematic scheme to identify and classify the cracking types of uniaxial compressive tests on specimens containing a single flaw was proposed. This method classified the cracking types into shear, tensile, and mix-mode cracks by analyzing the crack motion at the rupture moment with the aid of high-speed camera recording. In most of these previous experimental studies on rock/rock-like specimens containing a single flaw, the major focuses were the identification of macroscale

crack patterns and cracking paths and cracking type classifications. Only limited knowledge about the connection between the microscale crack accumulation and the macroscale fracture process has been obtained.

The fracture process zone in rock is normally much larger than that in metals or fine-grained ceramics (Nolen-Hoeksema & Gordon, 1987). However, presently, the relationship between the microscale fracture accumulation and the macroscale cracking in rock and rock-like materials remains unclear. A number of laboratory studies focusing on microscale observation of specimens containing preexisting flaw (s) have been conducted. Zhao et al. (1993) conducted real-time SEM observation on a marble plate (20 mm × 10 mm × 2.5 mm) containing a 45° inclined preexisting flaw (0.6-mm center hole diameter, 7.2-mm flaw length, aperture not mentioned) under loading. In their study, they concluded that the observed microcracks were mostly tensile in nature; cracks with detectable traces of shear slippage were very few. Wong and Einstein (2009b) conducted microobservation on specimens containing double preexisting flaws. According to their observation, a series of en-echelon microfractures developed along the future fracture coalescing path between two preexisting flaws prior to the macroscale fracture coalescence. Each individual microfracture in that series of en-echelon fractures was generally parallel to the loading direction. Such orientation suggested that they were tensile fractures. Cheng et al. (2016) conducted microobservation on specimens containing en-echelon artificially created preexisting flaws by fluorescent dye impregnation method. According to their observation, the microcrack density in the tensile stress zone was significantly higher than that of the shear stress zone throughout most of applied stress levels. Only at the stress very close to rock specimen failure, the microcrack density in shear zone significantly increased. Among these research studies, the major difficulties to establish the link between microscale fracture process and macroscale cracking by microscale observation are (1) the field of view was of limited size and scale, (2) the observations were discontinuously obtained in most cases, and, (3) in most cases, the loading tests had to be paused halfway for conducting the observation. Regardless of the preexisting flaw types (single, double, and en-echelon), the possible explanation for the small number of shear slippages in microscale (or lower microcrack density in shear stress zone) is that shear cracking can only appear in a comparatively very narrow time window, which is very close to the ultimate macroscale specimen failure. The scale-up process associated with the rapid expansion of fracture process zone into macroscale cracking was still not comprehensively observed and studied in laboratory tests.

This paper aims to provide a method to extend the presently available experimental observations on the fracture process of specimens containing a single preexisting flaw. In the present study, 16 channel acoustic emission (AE) system, camcorder, and high-speed camera are used to monitor the specimen under uniaxial compression loading. The AE data, camcorder video recording, and loading force-displacement record are synchronized. In the mesoscale, the fracture process is analyzed by AE source location and moment tensor inversion techniques. In the macroscale, the cracking types are classified based on the camcorder video recording and high-speed camera recording. By comparing camcorder video recording with AE source location and moment tensor inversion results, it is the first time the continuous picture on the white patch extension (see Appendix A for the detailed description of the white patch) and the accumulation and clustering of different types of cracks in mesoscale can be obtained in such type of test. The moment tensors of the AE sources provide insightful knowledge on the subscale fracture process. The rapid shifts on the subscale cracking types can help better distinguish much subtle and fundamental mesoscale changes in fracture process/scale-up stages than the traditional AE analysis solely based on AE hit rate, AE event rate, and energy release rate. The phenomena such as white patch initiation and widening, brightening dot appearance, and wrapped section appearance (explanation/description of these phenomena can be found in Appendix A) are the first time found to be attributed to specific mesoscale AE crack-type changes. New understanding on the role of stress drop on the development of fracture process zone has also been obtained. The changes in moment-frequency distribution can provide us with insightful information facilitating the understanding the relationship between laboratory scale tests and field scale earthquakes. One of the major foci of the present paper is to verify the observation capability of the proposed methods. The test results reveal that the AE source location closely matches the paths of white patches. Additionally, various new phenomena (possibly new stages) in the fracture process are observed. The distributions of the moment-frequency of AE sources also display distinctive features for different time sections. From rock engineering's perspective, the interest in laboratory tests on specimens containing a single preexisting flaw is initiated by simulating the geometry of joints, flaws, or tectonic scale faults embedded in a rock mass. From geophysicists' perspective, recent effort has been made to bridge the gap between the AE produced during small-scale laboratory
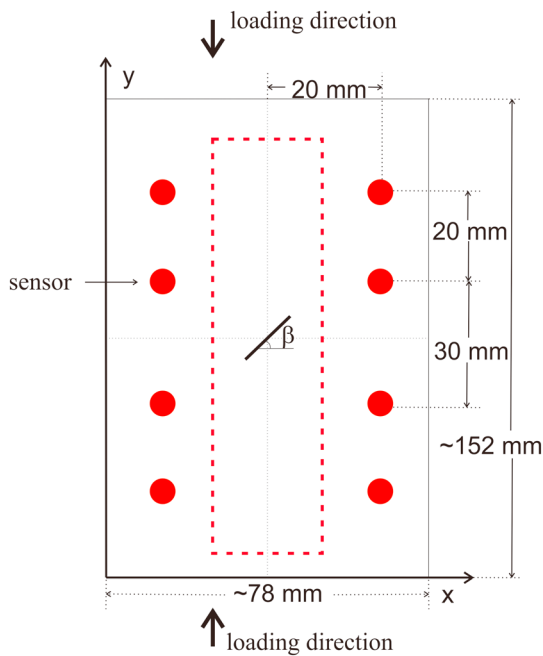
Figure 1. Sensor configuration and loading direction.

experiments and larger-scale man-made and natural earthquakes (Goodfellow & Young, 2014). The present experimental method together with the corresponding data analysis can enrich the understanding on both above-mentioned disciplines.

2. Methodology and Experimental Setup

2.1. Material Properties and Specimen Preparation

Carrara marble is selected for the present research due to its homogeneous and isotropic nature (Ramez & Murrell, 1964), comparatively small-ranging grain size, and its popularity in previous studies (Alber & Hauptfleisch, 1999; Cheng et al., 2015; Cheng & Wong, 2018; Edmond & Paterson, 1972). The Carrara marble is white in color, and it contains sparsely distributed gray bands or gray dots. These gray bands and dots consist of more than 50% calcite, and the other components are melanocratic minerals (Cheng et al., 2015). The average grain size is 50 to 300 μm. Taking into account the grain size and the sensor configuration (will be illustrated in section 2.2 and Figure 1), the source-to-sensor paths are approximately equal to or over 100 times the sources' characteristic sizes for most of fracture development stages. The overall rock porosity is very low at a value between 0.4% (Alber & Hauptfleisch, 1999) and 1.1% (Edmond & Paterson, 1972).

A group of prismatic Carrara marble specimens containing a single preexisting flaw at different inclination angle, β, are prepared. The original size of each specimen is 152 mm × 78 mm × 32 mm. The preexisting flaw is cut by the OMAX water jet. The flaw is designed to be 13 mm (length) × 1.6 mm (aperture). After the preexisting flaws are cut, the specimens are grinded smooth, particularly for minimizing the bulging effect of the water jet cutting and optimizing the sensor coupling. For this reason, the final size of each specimen subject to loading test is slightly different (Table 1a).

2.2. Acoustic Emission System

In the present study, the AE system manufactured by PAC (Physical Acoustic Corporation) is used. This system has two PCI-8 data acquisition boards and 16 signal channels. Sixteen Nano-30 sensors and 2/4/6 preamplifiers manufactured by PAC are used to monitor the AE from the specimens. All the sensors are attached onto the specimen by Loctite superglue, which provides stable and constant contact between the sensors and the specimens. No other couplant has been used. The sensor configuration with respect to the central preexisting flaw is presented in Figure 1. In each of the two faces (front and back) of the specimen, eight sensors are glued at identical X-Y planar positions. Before the loading test, pencil lead break, pencil scratching, and no-axial-force-applied piston up-and-down movement are repeatedly conducted to determine the data acquisition parameters such as threshold, HDT (hit definition time), and HLT (hit lockout time). Details of the present data acquisition parameters and sensor and preamplifier information are listed in Table 1b. A further explanation about the influences of these parameters on data acquisition is provided in Appendix A.

In this study, although all the sensors used are manufactured according to the respective factory standard, the exact AE data obtained may still be affected by the local surface condition of the specimen and the thickness of the couplant/glue applied between the specimen and sensors. Therefore, an in situ relative calibration is conducted before each test. The design and source type selection of the calibration are based on the work of Xiong and Wong (2017). The details of the calibration process are presented in Appendix A. This calibration has two purposes. First, it provides us with a location error estimation. Second, the first peaks of the received waveforms are used to calibrate the local/coupling effect of the sensors. For the source location, a homogeneous *P* wave velocity field model is used. Under the present flaw geometry and sensor configuration, the sensor array provides a 3-D mean error of 4.2 mm and a mean error of 1.9 mm in the thickness direction of the specimens within the central dash-line confined rectangular area in Figure 1 (much detailed explanation can be found in Appendix A). Based on the previous experimental experience and the video recording of the present tests, this area contains the majority of macroscale cracking path. The accuracy in this area is less

Table 1
Geometry of the Specimens, Acoustic Emission (AE) Data Acquisition Parameters, Loading Procedure, and Statistics on Waveform Numbers Before and After Filtering

a. Geometry of the specimens					
Flaw inclination angle (β)[a]	β = 90° (close to 90°)	β = 70°	β = 60°	β = 45°	β = 30°
Height (mm)	151.5	151.4	151.4	151.0	151.2
Width (mm)	75.4	78.9	78.9	78.8	78.3
Thickness (mm)	31.0	30.7	30.1	30.6	29.8
Flaw aperture (F/B)[b]	1.80/2.40	1.60/2.30	1.70/2.40	1.70/2.34	1.74/2.36

b. AE data acquisition parameters					
Parameter name	Threshold type	Threshold	HDT	HLT	Sampling rate	Preamplifier gain
Value	Floating	39 dB + 5	600 μs	600 μs	3 MHz	40 dB
Sensor operation range			125–750 kHz			
Sensor resonant frequency			300 kHz (in V/μbar reference unit)			

c. Loading procedure		
Loading stages	Stage 1	Stage 2	Stage 3
Load range	3–50 kN	50–100 kN	100 kN to failure
Loading rate	0.1 kN/s	0.002 mm/s	0.0001 mm/s

d. Statistics on waveform numbers before and after filtering					
Flaw inclination angle (β)	β = 90°	β = 70°	β = 60°	β = 45°	β = 30°
Original (before filtering)	92,322	101,285	114,034	158,918	66,597
After filtering	71,797	92,963	95,762	139,607	58,805

Note. HDT = hit definition time, HLT = hit lockout time.
[a]The flaw inclination angle β is measured from the horizontal direction as shown in Figure 1.   [b]F and B in the parentheses stand for aperture measured in the front and back of the specimen, respectively.

than 10% of the specimen size, but it is at least 10 times larger than the average grain size of Carrara marble. Details of the calibration process and results for all tests are provided in Appendix A.

2.3. Optical Monitoring System

For all tests, the front face of the specimens is continuously videotaped by a SONY camcorder (SonyHDR-XR150) and simultaneously monitored by a PHANTOM V310 high-speed video system (VRI-V310-16G-M). The latter is triggered manually to capture the images at the final failure moment. The frame rate and resolution of the high-speed camera system are set to be 10,000 fps and 352 × 600 pixels, respectively. With the 15-GB storage capacity of the high-speed camera, a high-speed camera video footage lasting 7.28 s can be recorded with the present setting.

2.4. Loading System and Test Procedure

The uniaxial compressive test is conducted on the MTS-815.02 concrete test system. The axial force and axial displacement are measured by a 250-kN force transducer and a pair of embedded linear voltage differential transducers in the axial piston, respectively. The accuracy for these two measurements are within 1.25 kN (0.413–0.428 MPa) and 0.01 mm (0.00660–0.00662% strain), respectively. The designed loading procedure is listed in Table 1c. Two folded plastic adhesive tapes with silicon grease lubrication between the folds are placed on the top and bottom of the specimens. Silicon grease lubrication is also provided between the platens and the tapes and between the tapes and the specimen. This treatment is to reduce the end friction between the specimen and platens. In addition, it can significantly reduce the influences of outside noise.

Before the start of the test, the specimen is preloaded with 3-kN axial force for over 20 min. This preloading slowly expels the extra silicon grease out from the gaps to minimize influences on the subsequent displacement measurement. The maximum adjustment rate of the axial piston valve is 1,024 Hz/s. This rate allows an accurate adjustment of the axial force loading at the postpeak stage. In each test, the MTS, the AE system, and the camcorder are manually triggered almost simultaneously. We estimate that the maximum time lapse related to the manual trigger of these three systems is within 0.4 s. Figure 2 shows the overall setup of the AE system, camcorder, high-speed camera, and MTS loading frame.
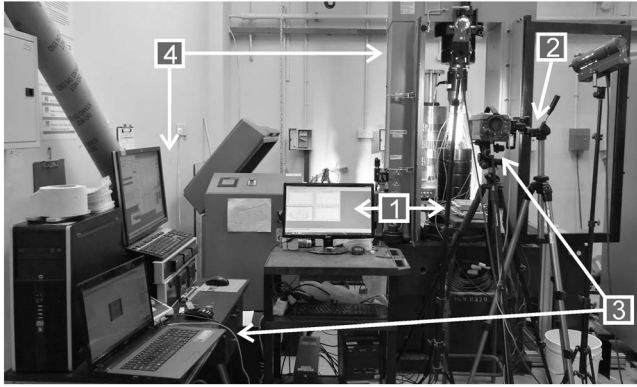
Figure 2. Assembly of the (1) acoustic emission system, (2) camcorder, (3) high-speed camera, and (4) MTS loading frame.

2.5. Data Processing and Analysis

Because of the complex nature of rock failure, it is unrealistic to only use the parameters provided by the PAC data acquisition software for distinguishing the signals of the elastic waves caused by true rock ruptures from the reflections and noise. Some enhancement methods must be supplemented to improve the signal selection. After the test, the AE waveforms are first filtered by the following criteria.

$$\begin{cases} T_{AIC} > T_{threshold} \\ 10\sigma_{avg} > Amp \\ DD > 0.05 \end{cases} \tag{1}$$

where T_{AIC}, $T_{threshold}$, σ_{avg}, "Amp," and "DD" stand for the onset time determined by the Akaike information criterion (T_{AIC}), the time at the first threshold crossing ($T_{threshold}$), the average signal level of the selected section from the preonset time (σ_{avg}), the peak amplitude of the waveform ("Amp"), and the DD parameter ("DD") based on a conjugated AIC model for estimating the accuracy of the autopicked onset time ("Carpinteri et al., 2012), respectively. The number of sampling points for calculating the DD value and the sampling points for calculating the average signal level of the selected section prior to the onset time are 50 and 10, respectively. The total number of the obtained signals and filtered signals is listed in Table 1d.

After the signal filtering, the onset time determined by AIC of the AE waveforms is used to seek source locations. Their corresponding first P wave amplitudes are used to calculate the time-independent moment tensors of the sources. The out-of-specimen source locations are discarded. Because of the "open" preexisting flaw, some first peaks are inevitably distorted if their source-to-sensor paths are intercepted by the flaw. A step of logic algorithm is implemented into the AE analysis program to judge whether the source-to-sensor path is intercepted by the preexisting flaw (see Appendix A). Once a signal is found to be of this condition, it will be rejected from the moment tensor inversion of the corresponding source. The moment tensors of those sources having over six signals whose source-to-sensor paths have not been intercepted by the preexisting flaw will be inverted. The source location algorithm used here is Simplex algorithm, in which the optimization function between the observed onset time and the calculated onset time (equation (2)) will be minimized. As the algorithm iterates, the initial guess points of source location would shrink to a point where outputs the minimal residual (ε) between the observed time and calculated time.

$$\varepsilon = \frac{1}{n}\Sigma_{i=1}^{n}\text{abs}(T_{obs} - T_{cal})_i \tag{2}$$

where T_{obs} and T_{cal} are the observed and calculated sensor onset time, respectively.

The 3-D SiGMA (Ohtsu, 1995) moment tensor inversion method is used in this study. In this method, the relationship between the observed AE amplitudes and the source moment is expressed as equation (3),

$$A(x) = Cs\frac{R_e(t,r)}{R}r_p M_{pq} r_q \tag{3}$$

where $A(x)$ is the observed amplitude; Cs is the magnitude of the sensor response including material constants, which is obtained through in situ sensor calibration (Appendix A); R is the distance from the source to the sensor; r_p and r_q are the directional cosine; and M_{pq} is the moment tensor of the source. $R_e(t,r)$ is the reflection coefficient which is expressed as (Ohtsu, 1995)

$$R_e(t,r) = \frac{2k^2 a\left[k^2 - 2(1-a^2)\right]}{\left[k^2 - 2(1-a^2)\right]^2 + 4a(1-a^2)\sqrt{k^2 - 1 + a^2}} \tag{4}$$

where t represents the orientation vector of sensor sensitivity which is assumed to be the normal vector of a sensor, $k = {}^{v_p}\!/_{v_s}$ is the ratio of P wave velocity and S wave velocity, and a is the scalar product of vectors r and t.

Once the moment tensor of an event is obtained, the Eigenvalues and Eigenvectors of the moment can be solved. The moment tensor decomposition procedure is accomplished by equation (5) (Ohtsu, 1995),

$$\begin{cases} \dfrac{e_1}{e_1} = X + Y + Z \\[2mm] \dfrac{e_2}{e_1} = 0 - 0.5Y + Z \\[2mm] \dfrac{e_3}{e_1} = -X - 0.5Y + Z \end{cases} \tag{5}$$

where e_1, e_2, and e_3 are the maximum, intermediate, and minimum Eigenvalues, respectively; X, Y, and Z are the shear component, deviatoric component, and hydrostatic component of the source moment, respectively. The cracking motion vector (l) and the normal vector of the crack surfaces (n) can be obtained by equation (6),

$$\begin{cases} \text{normalized}(e_1) = \text{normalized}(l + n) \\ \text{normalized}(e_2) = \text{normalized}(l \times n) \\ \text{normalized}(e_3) = \text{normalized}(l - n) \end{cases} \tag{6}$$

The P wave velocity and S wave velocity required for this moment tensor inversion are measured by a PROCEQ ultrasonic tester together with the calibration process prior to each compression test (see Appendix A). The signal filters, AIC onset time determination, and autopicking of the first peaks, source location, intercepted signal rejection, and moment tensor inversion and decomposition procedure used in this paper are implemented in a suite of in-house MATLAB programs.

3. Experimental Results

The experimental results of optical observation system, the AE system, and the MTS mechanical test system will be presented separately in this section. The comparison of the results among these three systems will be discussed for each test in section 4.

3.1. Optical Observation Results

Optical recordings provided by the camcorder and the high-speed camera are used to characterize the macroscale cracking behavior of the specimens. The crack classification follows Wong and Einstein (2009a), which contains three types of tensile crack, three types of shear crack, and one type of mixed shear-tensile crack (Figure 3). In this classification, not only the crack inclination angle with the axial loading direction but also the motions of the two crack surfaces at the cracking moment are used to characterize the crack type. The observation results of the present study are analyzed and listed in Table 2.

The above crack classification results are generally comparable with the results presented by Wong and Einstein (2009a). Some differences between them may be attributed to the subjectivity of distinguishing a crack opening from the formed white patches.

3.2. Mechanical Results

The mechanical stress and strain versus time curves are plotted in Figures 4a–4e. The stress is calculated from the axial force divided by the specimen's top/bottom area. The strain is calculated from axial displacement divided by the specimen height. In these figures, all the specimens have a postpeak stage lasting from several minutes to almost 20 min. In several tests (β = 70°, 60°, 45°, and 30°), the stress drops of the post peak stages have one or several interceptions of local stress buildup or local stress-hold (the stress level is neither obviously increasing nor decreasing for a period). Tracing back to the video recordings, the timing of these stress drops after the stress-hold or local stress buildup are always accompanied by the formation of a new white patch, an obvious extension of the white patch, and/or the crack opening of some white patches.

3.3. AE Source Location and Moment Tensor Inversion Results

The AE source location results are first plotted into histograms (bins of 500) against time (Figure 5). Later, the experimental time is separated into different time sections based on the changes in these AE event
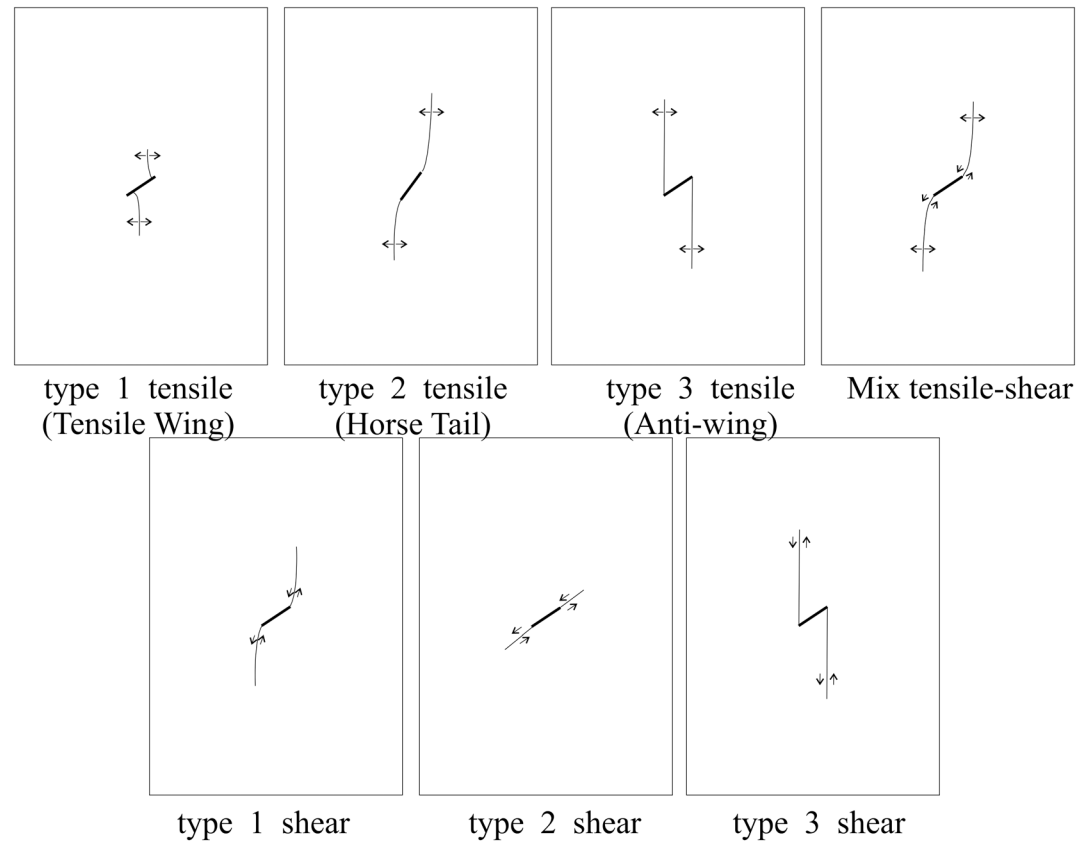
Figure 3. Crack-type classification, redrawn after Wong and Einstein (2009a).

histograms (changes from rising trend to falling trend or falling trend to rising trend). The AE source locations and the moment tensor inversion results of different time sections are presented separately. The analysis is combined with the stress and strain versus time curves and the camcorder recording. For instance, around the separating points of these time sections, the extension of white patches or macrocrack opening and the local stress drop or stress-holding appear along some sequences. This will be discussed further in the next section. The division of these time sections is subjective to certain extent because of the bin number used in the histograms. However, this subjectivity is negligible as compared with the much longer test duration. The crack-type classification is based on the moment tensor decomposition result. Relative AE moment is calculated directly from the moment tensors based on equation (7). This calculation was used for interpreting the seismic moment by Zhu and Ben-Zion (2013).

Table 2
Macroscale Crack-Type Classification

Flaw inclination angle (β)	Crack types						
	Type 1 tensile	Type 2 tensile	Type 3 tensile	Mixed tensile-shear	Type 1 shear	Type 2 shear	Type 3 shear
Close to 90		C*			C		
70	C	C*				C	
60	C	C*			C		
45	W.P.	C*	W.P.	C	C		
30	W.P.	C*	C		C		C

Note. The flaw inclination angle (β) is to the horizontal direction (refer to Figure 1). W.P. = white patch developed; C = crack of the respective type developed; * = first open crack.
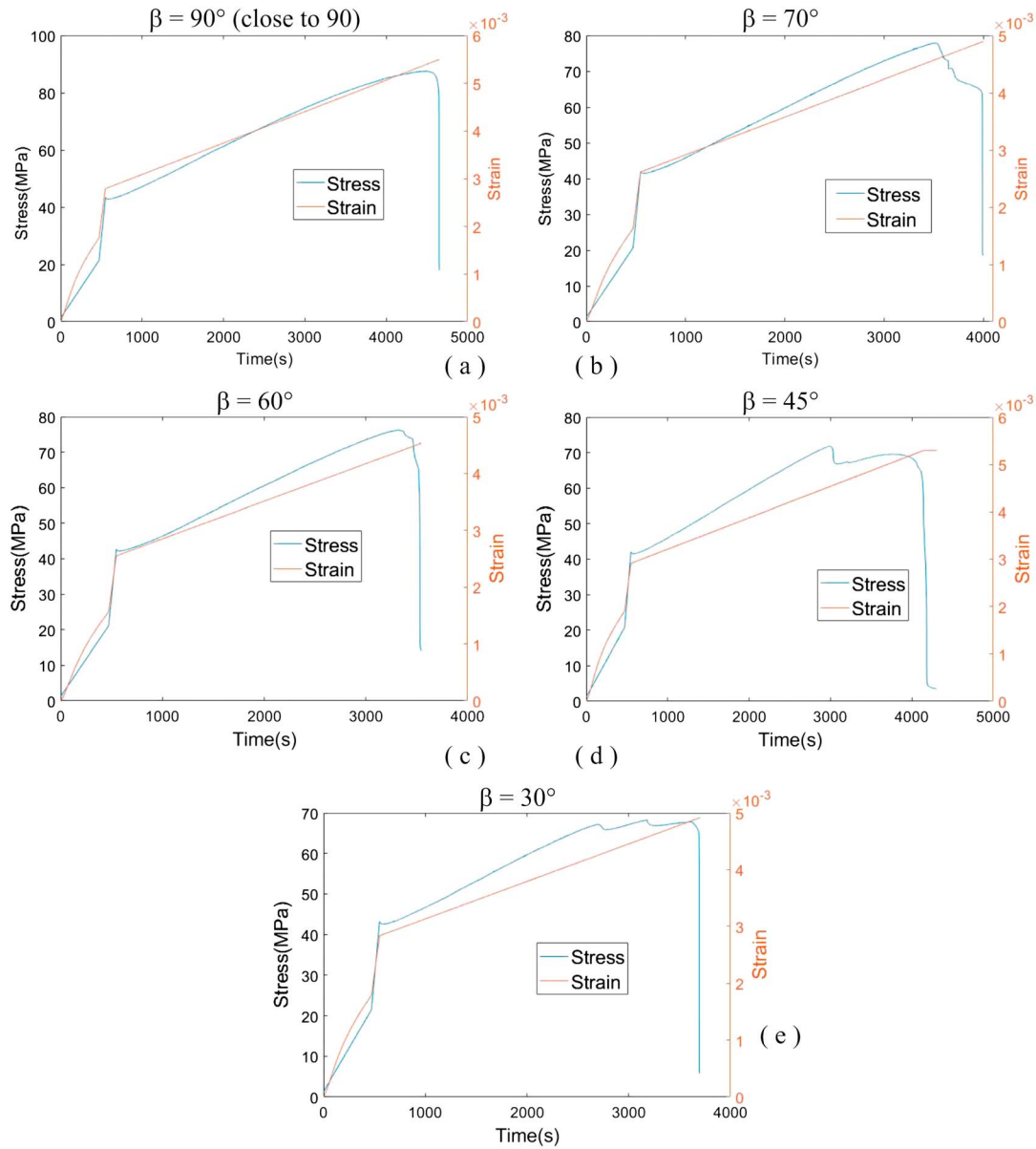
Figure 4. Stress and strain versus time curves for (a) β = 90°, (b) β = 70°, (c) β = 60°, (d) β = 45°, and (e) β = 30°. The flaw inclination angle β is measured from the horizontal direction as shown in Figure 1.

$$M = \sqrt{\frac{M_{ij}M_{ij}}{2}} \tag{7}$$

The time sections divided according to the histogram changes for each test and the corresponding number of source locations (in parentheses) are listed in Table 3. The sources for each time section and the corresponding cracking motions and cracking planes of the sources are presented separately in Figures 7–11. The presentation of the cracking motion and cracking normal (see the illustration in Figure 6e) followed the convention of Ohno and Ohtsu (2010). Figures 6a–6c illustrate the elements used to represent the different crack types—tensile (blue), shear (red), and mixed-mode (green) cracks, respectively. The selected classification thresholds are, $\frac{X}{X+Y+Z} > 0.6$ for the shear crack, $0.4 < \frac{X}{X+Y+Z} < 0.6$ for the mixed-mode crack, and $\frac{X}{X+Y+Z} < 0.4$ for the tensile crack, respectively (Ohtsu, 1995). The preexisting flaws for all tests are presented along with the AE source locations and moment tensor inversion results as a solid line shown in Figure 6d.
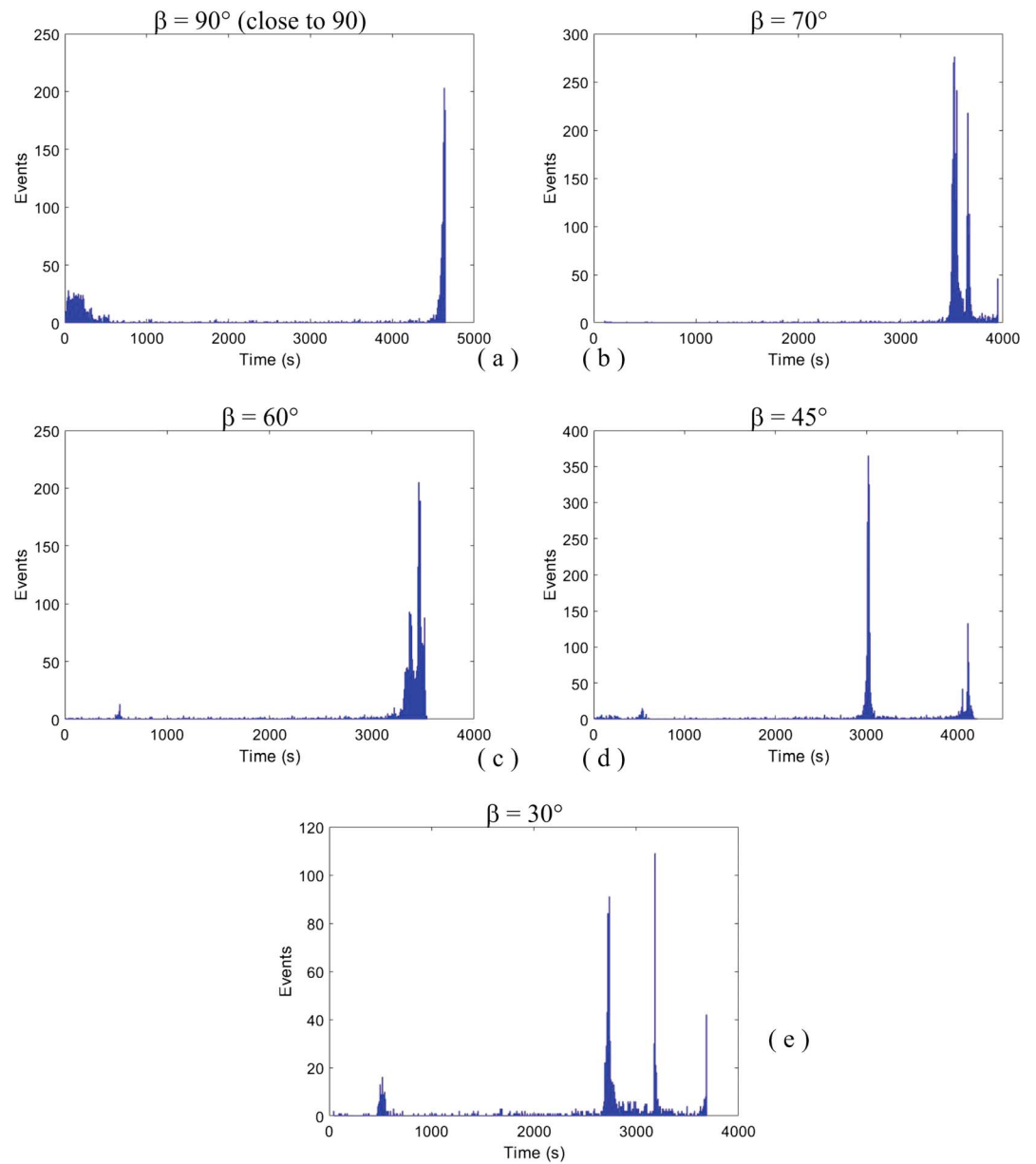
Figure 5. Histogram plots of the acoustic emission source location for all tests.

The definitions of crack normal and crack motion are presented in Figure 6e. The screenshots of the camcorder videos at the end points of the time sections and the high-speed camera image (s) at the final cracking moment are supplemented below the source location pictures. The temporal evolutions of AE crack-type ratios are calculated according to the AE crack-type classification using the above-mentioned

Table 3
Divided Time Sections and Corresponding Number of Source Locations (in Parentheses)

| β (°)	Section 1	Section 2	Section 3	Section 4	Section 5	Section 6	Section 7
90	0–550 s (675)	550–4,300 s (165)	4,300–4,565 s (86)	4,565 to end (856)			
70	0–3,430 s (176)	3,430–3,530 s (996)	3,530–3,615 s (817)	3,615–3,665 s (460)	3,665 to end (415)		
60	0–3,070 s (242)	3,070–3,370 s (471)	3,370–3,420 s (440)	3,420–3,470 s (658)	3,470 to end (626)		
45	0–2,650 s (359)	2,650–3,025 s (1,050)	3,025–3,100 s (442)	3,100–3,830 s (174)	3,830–4,060 s (160)	4,060–4,120 s (231)	4,120 to end (169)
30	0–2,650 s (228)	2,650–2,740 s (376)	2,740–3,040 s (221)	3,040–3,190 s (180)	3,190–3,550 s (101)	3,550 to end (82)	
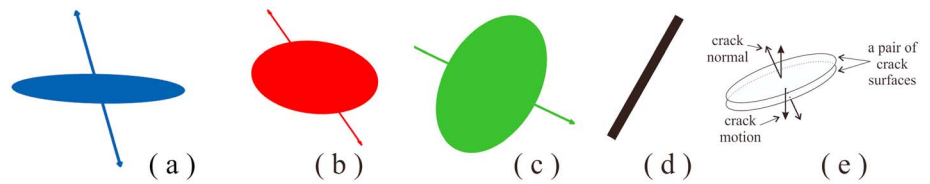
Figure 6. Illustration of three crack-type presentations, (a) tensile crack, (b) shear crack, (c) mixed-mode crack, (d) preexisting flaw (color figure online), and (e) crack normal and crack motion.

thresholds. AE crack-type ratio is defined as the number of events of a certain crack type included by the moving averaging window (50 events in the present study) divided by the total event number included in that moving averaging window.

Figures 7–11 show the source location and moment tensor inversion results of each test, together with the corresponding video screenshots at the end of each time section. A preliminary comparison between the AE clustering results and the video screenshots reveals that the extension of the macroscale cracks is
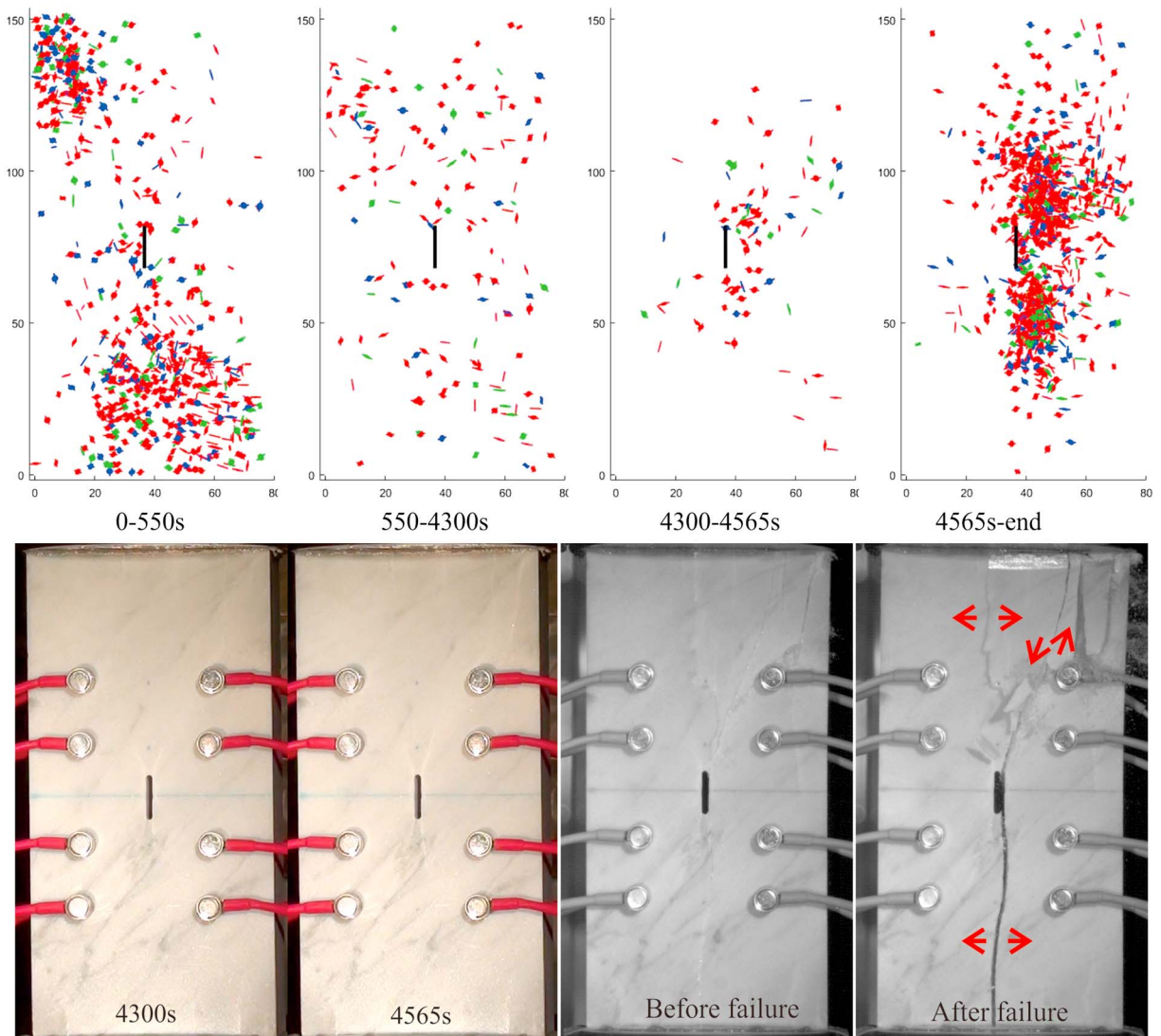

Figure 7. (top) Acoustic emission source locations and moment tensor inversion results of each time section. (bottom) Corresponding screenshots for β = 90° test (color figure online).
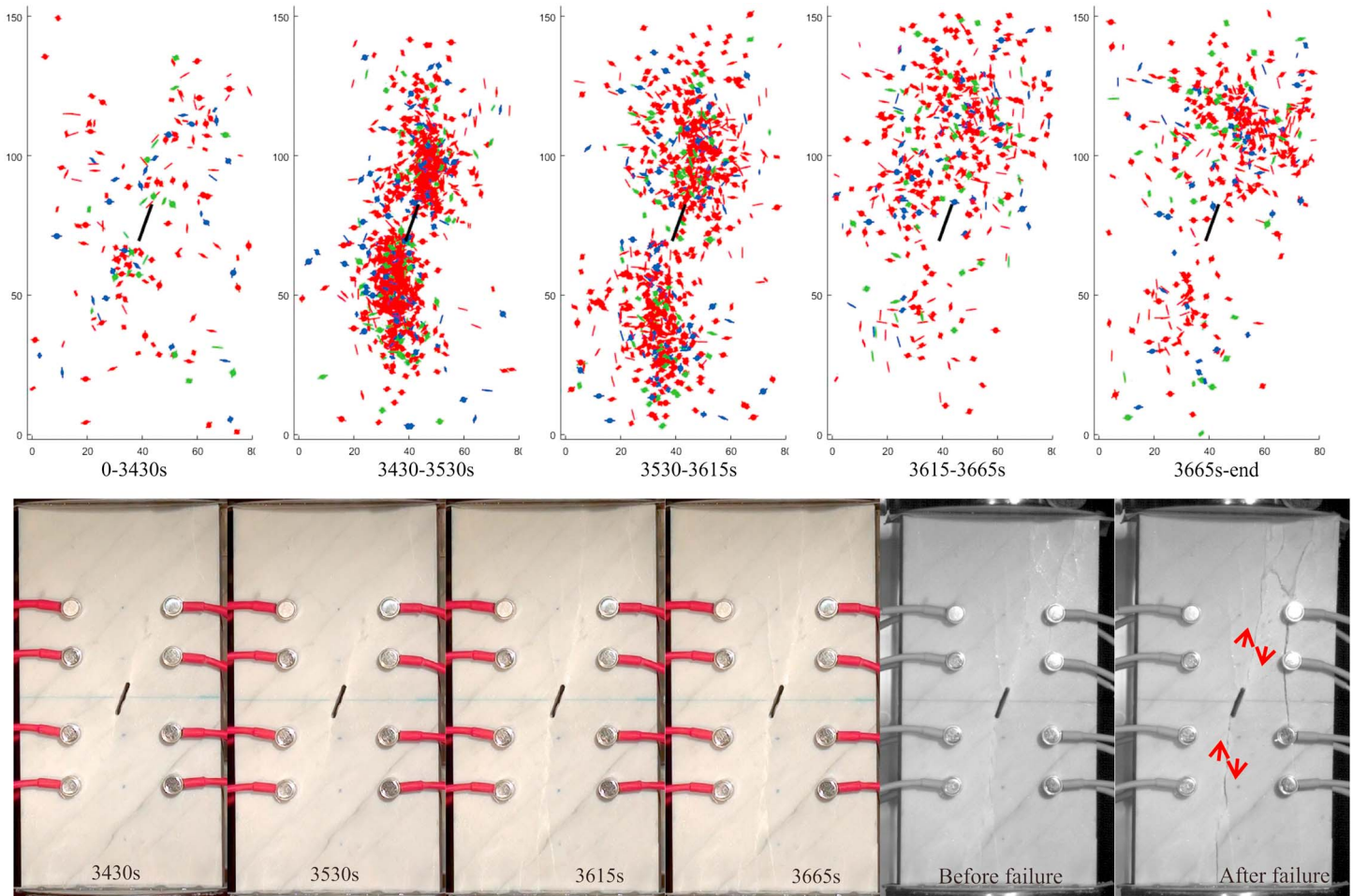
Figure 8. (top) Acoustic emission source locations and moment tensor inversion results of each time section. (bottom) Corresponding screenshots for β = 70° test (color figure online).

normally accompanied by the formation of AE clusters. For the first fracture propagation (the first time when the fracture initiates and propagates toward the top and bottom specimen boundaries), the center lines of the AE clusters closely match the cracking paths/white patches. After the propagating fracture reach the specimen boundaries, the AE source locations appear scattered for the later stages (time sections). A further discussion on source locations for each test will be provided in the following section. For the β = 30° test, one sensor prematurely detaches from the specimen. The signals obtained by this sensor (sensor 3) after its detachment are excluded from the source location analysis.

3.4. Temporal Evolutions of AE Crack-Type Ratios and Relative AE Moment-Frequency Distributions

The temporal evolutions of crack-type ratios of β = 90°, 70°, 60°, 45°, and 30° tests are shown in Figures 12a, 13a, 14a, 15a, and 16a, respectively. These ratios are based on moving average of 50 events for better elucidating the changes along the testing time. Figures 12b, 13b, 14b, 15b, and 16b present the relative AE moments of each test against time in a linear-log plot. The AE moment of each individual source is calculated by equation (7). In these figures, the large moment events always occur at a time of high AE event concentration. The relative AE moment-frequency distributions of different time sections are shown in a log-log plot in Figures 12c, 13c, 14c, 15c, and 16c. For different flaw inclination angles, the evolutions of the crack-type ratios are different. The changes on the crack-type ratio curves seem to be related to the appearance of the white patches, or/and white patch extension, or crack opening as observed in the camcorder video recordings. In (c) of Figures 12–16, the inclinations (slopes) of the curves for each time section are remarkably different. A brief discussion of this issue will be provided in section 5.
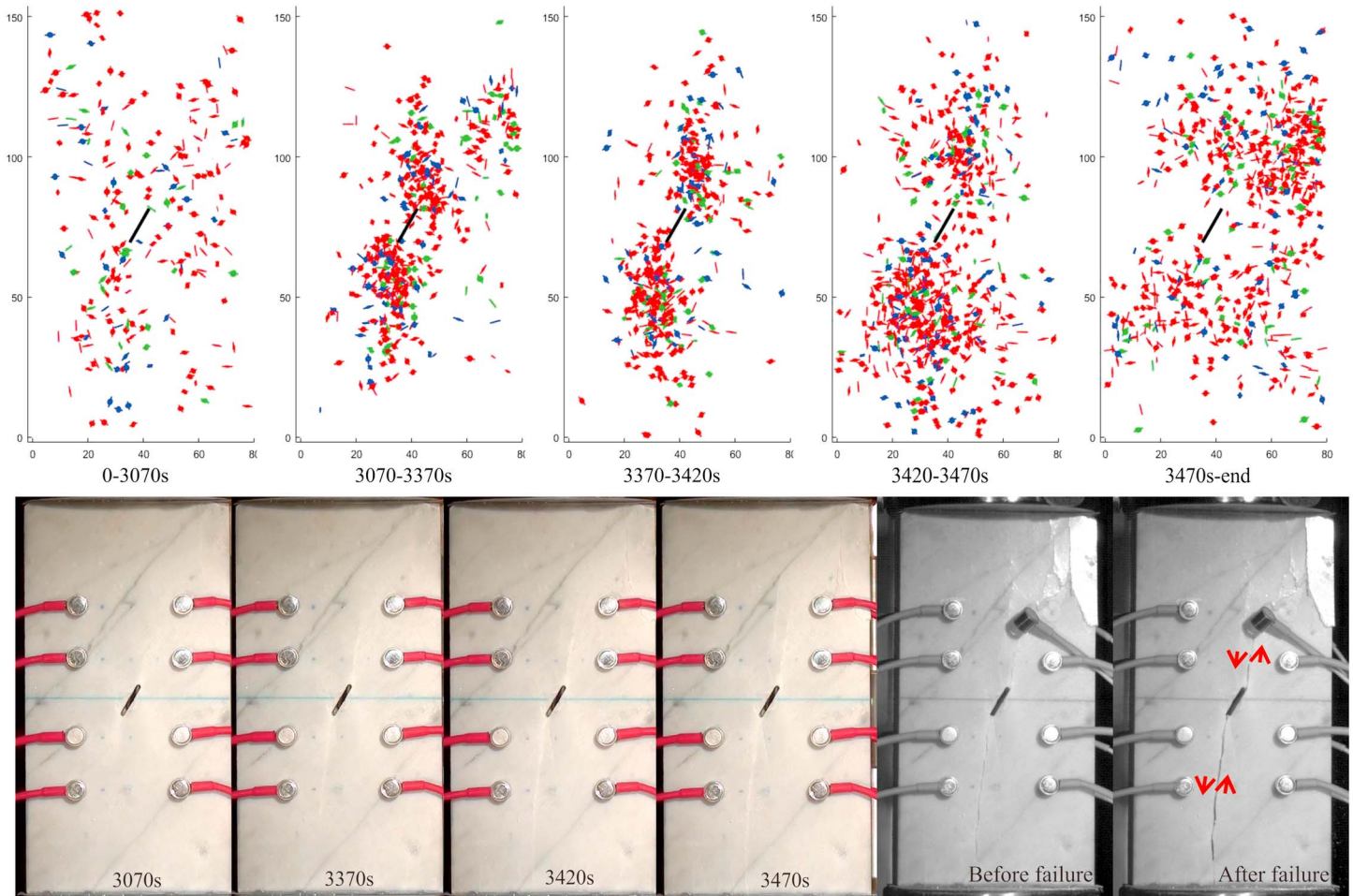
Figure 9. (top) Acoustic emission source locations and moment tensor inversion results of each time section. (bottom) Corresponding screenshots for β = 60° test (color figure online).

4. Cross Comparison Among the Results Provided by Different Systems

Since the MTS loading system, the AE system, and the camcorder are triggered simultaneously, comparisons between the observed results from different systems are possible. In the following subsections, different sets of results from each individual test will be compared as follows. First, the three crack-type ratios and the stress curve versus the same time line are plotted on the same graph. Second, identify the changing points on crack-type ratios. Third, the changing points on crack-type ratios and the separation points between time sections are indicated and labeled in the plots. The changing points on crack-type ratios (named as CTC_i for crack-type changing point at i second in the following description) are indicated by star marks along the crack-type ratio curves. Each crack-type changing point has been labeled with a number, and the corresponding time of the crack-type changing point has been indicated by a legend beside the plots. The time sections are indicated and labeled by "S_i" (i stands for the number of time section) at the top of plots accompanied with vertical blue dashed-dotted lines separating these time sections (named as section i-j for the separation point between i and j time sections in the following description). Forth, check the camcorder video recordings for the corresponding time periods.

To avoid the influence of the time lapse between different systems, namely, the camcorder, the AE system, and the MTS loading system, the resolution for picking the changing points is selected to be 5 s. This selection is over 10 times the estimated time lapse between different systems (0.4 s). As such, the related phenomena on different systems can be correlated temporally. In most identified changing points, camcorder screenshots are provided for better illustration. The discussion and conclusions based on the experimental results in
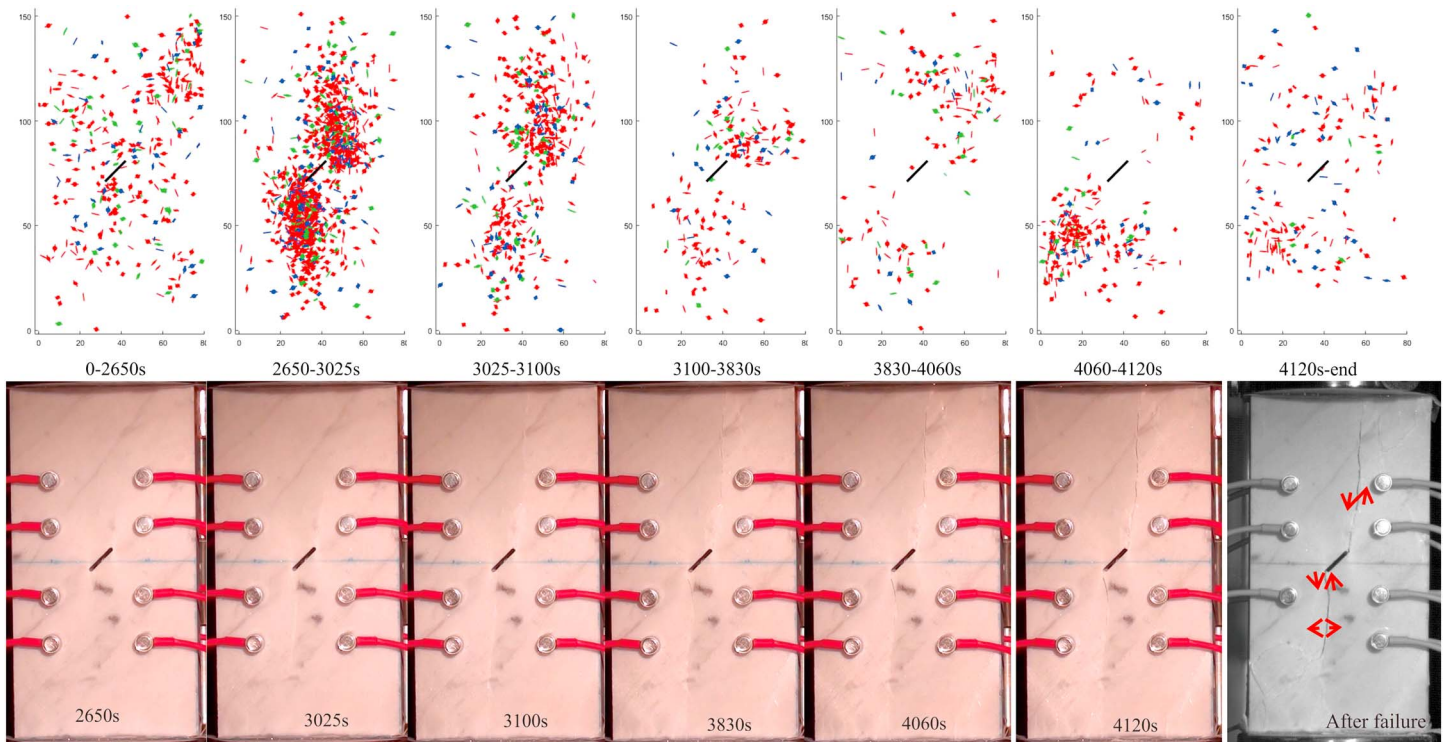
Figure 10. (top) Acoustic emission source locations and moment tensor inversion results of each time section. (bottom) Corresponding screenshots for β = 45° test (color figure online).

section 3 and those cross comparisons in section 4 will be presented in section 5. In the following subsections, the phenomena of β = 70° test will be described in detail as an illustration of the cross-system comparison. The detailed description on other tests is not provided due to the limitation of space here. The results of the cross-system comparison for all tests will be summarized in Table 4.

4.1. Comparison on β = 70° Test

The AE source location and moment tensor inversion analysis of this test is divided into 5 time sections based on the AE event histogram (Table 3). Because the remarkable (1) changes of AE crack-type ratios, (2) changes of AE histogram, (3) stress nonlinearity, and (4) white patch extension and crack opening all occur late during the entire course of loading, the plot from 3,200 s until the end is enlarged for clearer illustration (Figure 17a). The description and analysis below focus on the final stage of loading.

As observed in the camcorder recording, at crack-type changing point 3,290 s (will be referred to as CTC3290 thereafter, labeled as 1 in Figure 17a), the white patches of horse tail trajectory (type II in Figure 3) initiate from the two flaw tips (Figure 17b). The stress curve fluctuates slightly around and after CTC3290 (approximately from 3,290 to 3,330 s; see Figure 17a). This fluctuation is larger than the measurement error of the force transducer (1.25 kN ≈ 0.5 MPa). However, the fluctuation range is small when compared with the contemporary axial stress. From CTC3290 to CTC3445 (labeled as 2 in Figure 17a), the ratio of shear crack generally declines, while as observed in the camcorder recording, the white patches become longer (Figure 17b). Just 15 s prior to CTC3445, the AE event histogram begins to rise at section 1-2 (vertical blue line between S1 and S2 in Figure 17a; see also in Table 3 and Figure 5b). From CTC3445 to CTC3480 (labeled as 3 in Figure 17a), the ratio of shear crack rises, while the white patches extend slightly, becoming wider and much longer (Figure 17b). At CTC3480 (labeled as 3 in Figure 17a), the length of the white patches becomes comparable to or longer than the length of the preexisting flaw.

From CTC 3480 to CTC 3565 (labeled as 4 in Figure 17a), the crack-type ratios shift significantly. During this period, the white patches remarkably extend toward the upper and lower specimen boundaries at approximately 70° inclination (Figure 17b). The first peak of AE event histogram (vertical blue line between S2 and S3
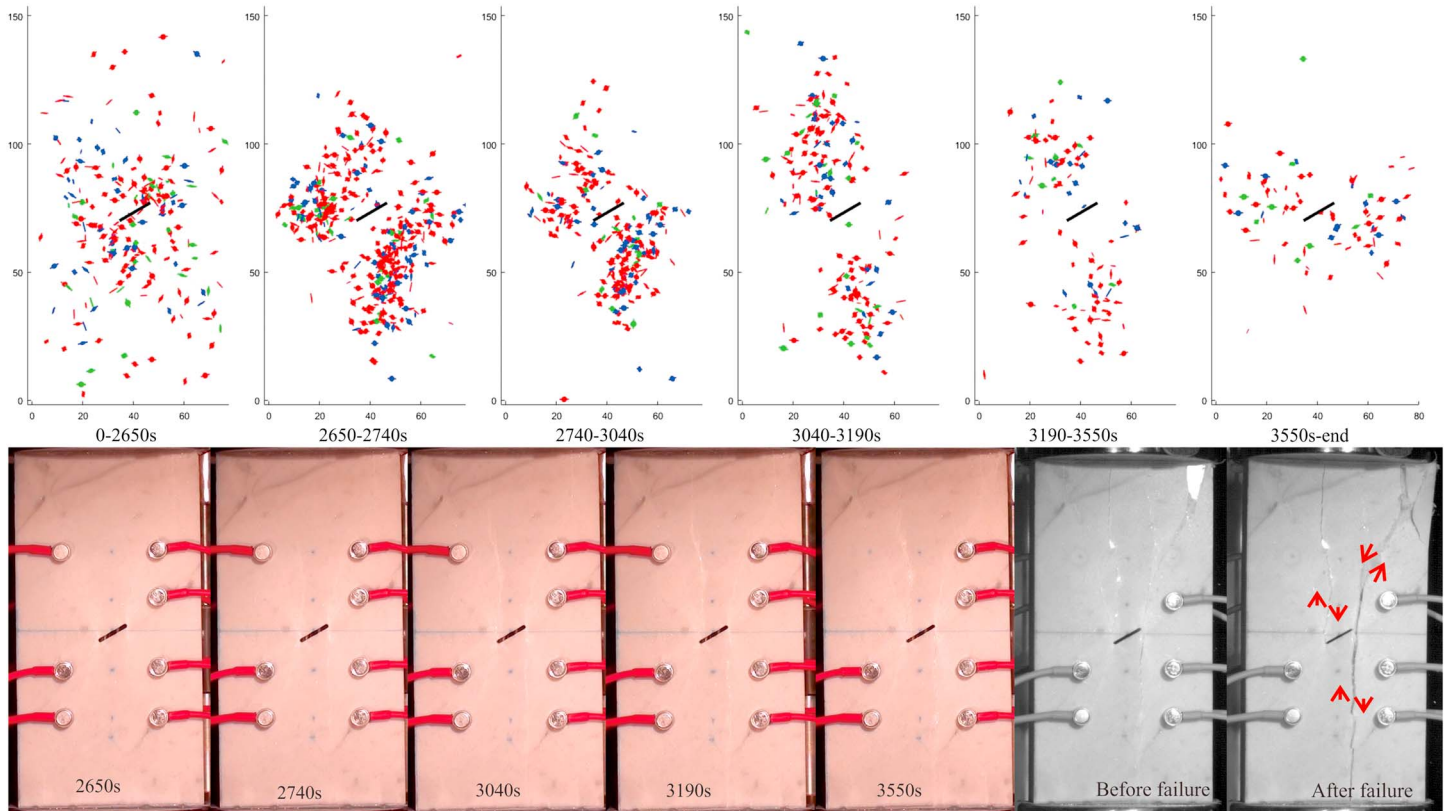
Figure 11. (top) Acoustic emission source locations and moment tensor inversion results of each time section. (bottom) Corresponding screenshots for β = 30° test (color figure online).

in Figure 17a; see also in Table 3 and Figure 5b) is close to the midpoint between CTC3480 and CTC3565. The time of section 2-3 (vertical blue line between S2 and S3 in Figure 17a) is coincident with the peak of stress. From CTC 3565 to CTC 3595 (labeled as 5 in Figure 17a), the ratio of shear crack declines again. At CTC3595, the white patches reach specimen boundaries (Figure 17b), while an inflection point on the stress curve appears coincidently at CTC3595.

From CTC3595 to CTC3605 (labeled as 6 in Figure 17a) a short rise-and-drop for the ratio of shear crack occurs. At CTC3605, a new vertical white patch subtly appears at a distance away from the horse tail white patch of the upper part of the specimen (Figure 17b). At the same time, the secondary tensile wing (type I in Figure 3) white patch also subtly appears at the upper part of the specimen.

From CTC3605 to CTC3640 (labeled as 7 in Figure 17a), the ratio of shear crack rises again, while all the white patches become wider (Figure 17b). Some sections of the white patches become wrapped inward or outward as shown in the screenshot at CTC3640 (Figure 17b). Around 10 s after CTC3605, the AE event histogram begins to rise at section 3-4 (vertical blue line between S3 and S4 in Figure 17a; see also in Table 3 and Figure 5b). The ratio of shear crack enters another abrupt phase again from CTC3640 to CTC3675 (labeled as 8 in Figure 17a), while the screenshot at CTC 3675 is very similar to the screenshot at CTC3640 (Figure 17b). Some brightening dots occur sparsely along the path of the white patches/cracks within this short period. The second peak of AE event histogram (section 4-5, vertical blue line between S4 and S5 in Figure 17a; see also in Table 3 and Figure 5b) occurs between CTC3640 and CTC3675. Within this period, the stress first undergoes a sharp drop, which then becomes stable for a while and begins to build up again. The peak of this local stress buildup appears coincident with CTC3675 (Figure 17a).

From CTC3675 to CTC3750 (labeled as 9 in Figure 17a), as observed in the camcorder recording, the frequency of brightening dots' appearance first rises and then decreases; wrapped sections gradually occur along the white patches and replace the brightening dots (can be partially revealed by Figure 17b). The inflection point on the stress curve within this period (Figure 17a) appears to be corresponding to the
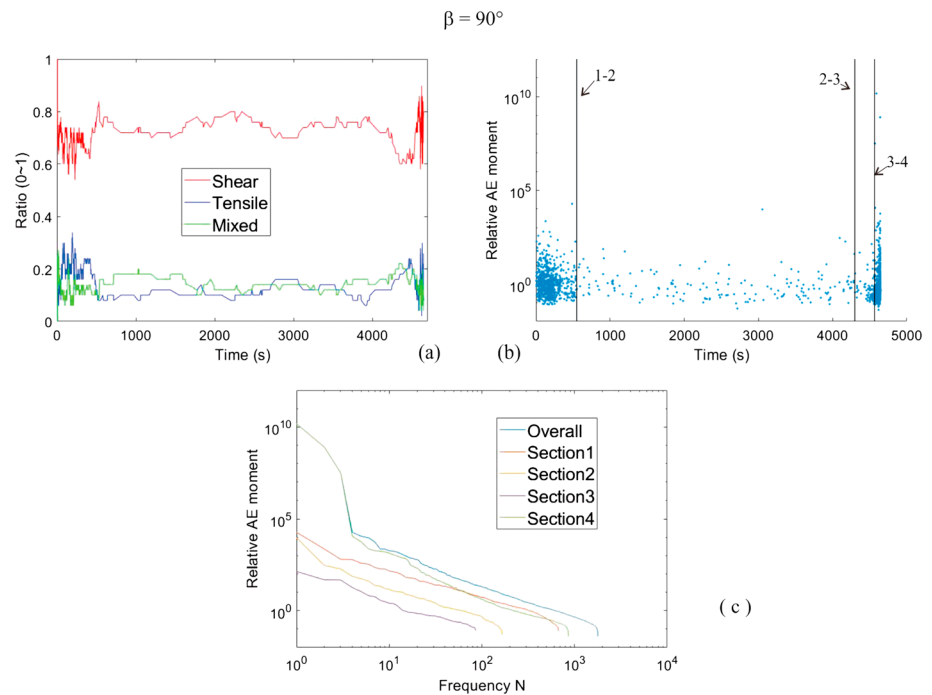
Figure 12. (a) Acoustic emission (AE) classified crack type, (b) relative AE moment, and (c) relative AE moment-frequency distribution for β = 90° test.

transition point that the appearance of wrapped sections becomes the dominant phenomenon of the fracture processes instead of the appearance of brightening dots.

From CTC3750 to CTC3810 (labeled as 10 in Figure 17a), as observed in the camcorder recording, some rock materials detach from some severely wrapped sections and the wrapped sections enlarge (Figure 17b). Some
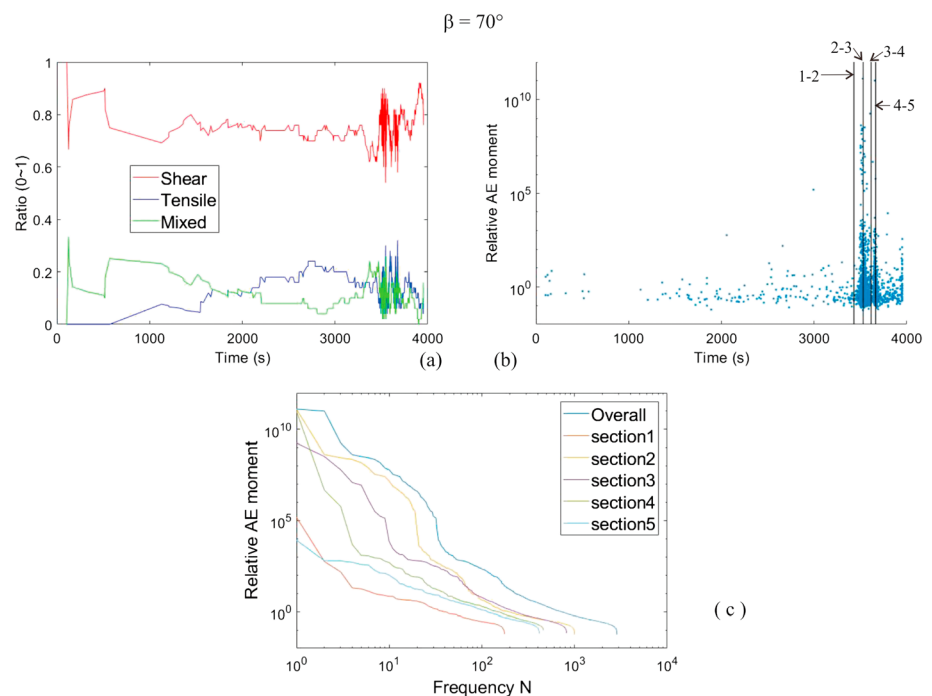

Figure 13. (a) Acoustic emission (AE) classified crack type, (b) relative AE moment, and (c) relative AE moment-frequency distribution for β = 70° test.
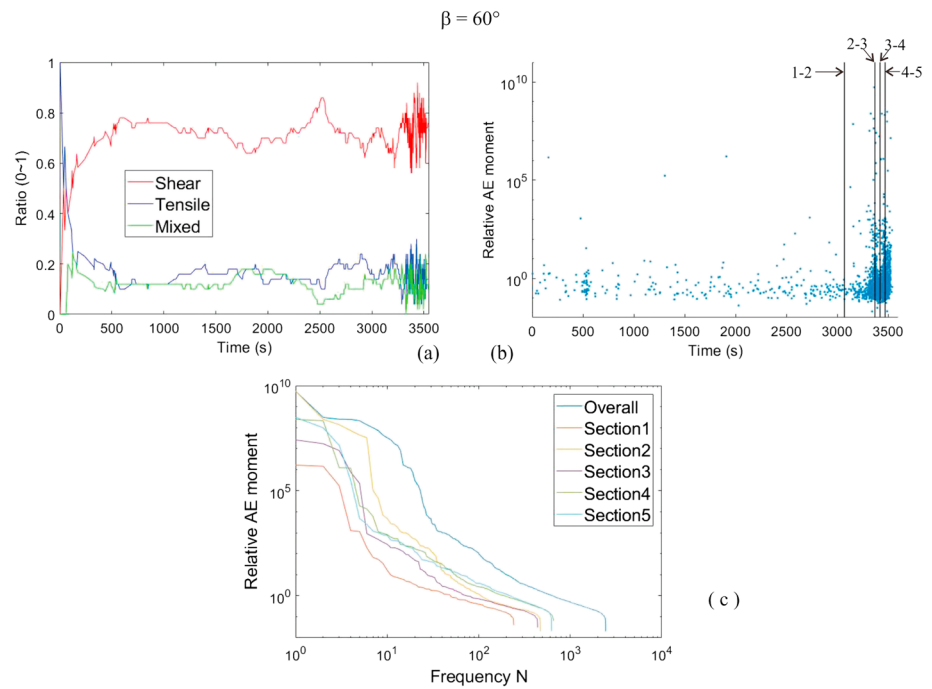
Figure 14. (a) Acoustic emission (AE) classified crack type, (b) relative AE moment, and (c) relative AE moment-frequency distribution for β = 60° test.

wrapped sections begin to connect with each other. From CTC3810 to CTC3910 (labeled as 11 in Figure 17a), the ratio of shear crack rises again, while no significant change in camcorder recording within this period is observed. As the test approaches the end, the ratio of shear crack declines again after CTC3910, showing a preferential development of tensile cracks prior to the final rupture.
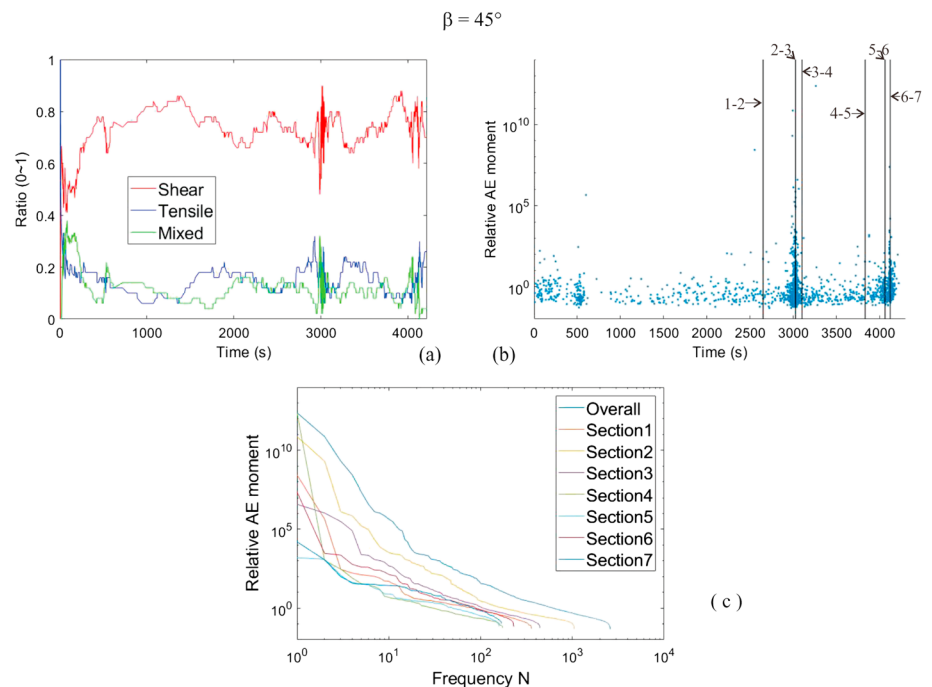

Figure 15. (a) Acoustic emission (AE) classified crack type, (b) relative AE moment, and (c) relative AE moment-frequency distribution for β = 45° test.
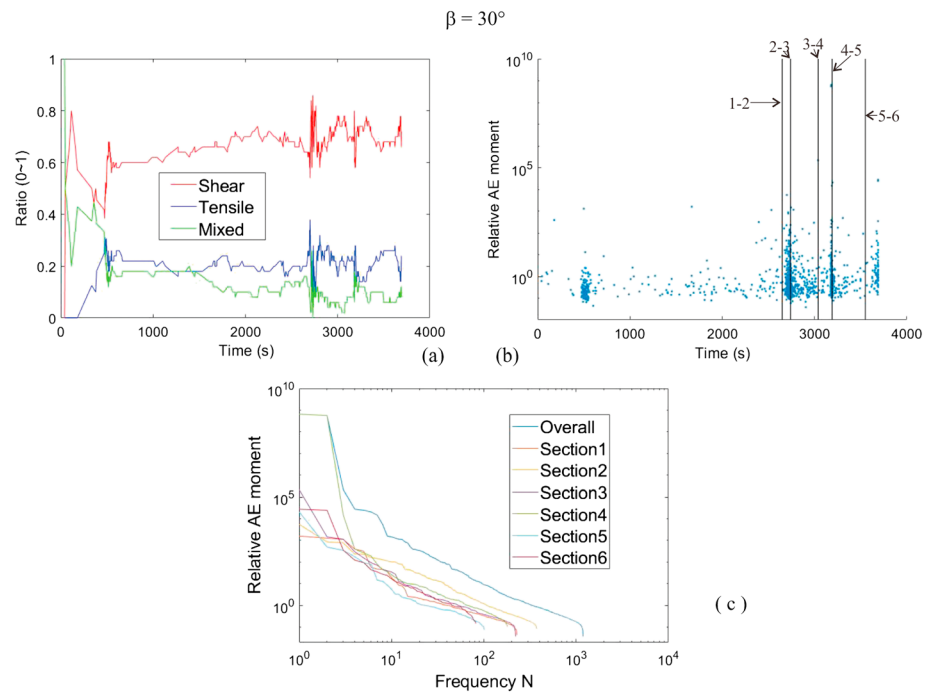
Figure 16. (a) Acoustic emission (AE) classified crack type, (b) relative AE moment, and (c) relative AE moment-frequency distribution for β = 30° test.

4.2. Comparison on β = 90°, 60°, 45°, and 30° Tests

As stated in the previous part of this section, detailed description on β = 90°, 60°, 45°, and 30° tests will not be provided in this paper due to the space limit. Only the corresponding figures for cross comparison are presented below (Figures 18–21).

5. Discussion

5.1. Mechanical Stress Drops, Perturbations, and Inflection Points on Stress Curves and Corresponding Mesoscale AE Crack-Type Changes

From the mechanical perspective, new evidence of the correlations between the accumulation of microscale-mesoscale cracks and the macroscale stress behavior (such as local stress peaks, sharp stress drops, and the inflection points on stress curves) are found. In all five tests (Figures 17a, 18a, 19a, 20a, and 21a and Table 4), the stress changes are coincident with AE crack-type ratio changes and/or AE histogram changes (for instance, in β = 70° test, the time of first stress peak is coincident with the separation point between time section 2 and time section 3 [AE peak at 3,530 s], CTC3595 is coincident with a stress inflection point characterized as stress drop deceleration, and the second stress peak is coincident with CTC3675). As the changes in stress curves are believed to be the macroscale phenomena caused by the subscale crack accumulations, this sequence further evidently suggests the close correlation between macroscale stress changes and the shifting of subscale AE fracture mechanism.

Besides the major changes in stress curves, the proposed method is advantageous to the discovery of the subtle changes on stress and fracture process. Some subtle stress changes/perturbations, such as the stress perturbation around and after CTC3290 in β = 70° test (Figure 17a) and the small drop at CTC3215 in β = 45° test, are also identified by the crack-type changes. These small stress changes, which are much smaller than the major stress changes in the stress curves, indicate the transitions of plausible new stages in the fracture processes when they are characterized by AE crack-type changes. For β = 70° test, CTC3290 suggests the decline of the influence of the preexisting flaw and the dominance of the initiated fracture in subsequent fracture extension. The physics of the fracture initiation from an open preexisting flaw is obviously different from the fracture extension from the initiated fracture. For β = 45° test, brightening dots vividly appear before

Table 4
Comparison on β = 90°, 70°, 60°, 45°, and 30° Tests

Inclination angle β	Inc-W.P.	W.P. > flaw	σ peak	1st R.B.	1st Abt phase	Other phenomena
90	↑CTC3920	CTC3920↓4425	CTC4460	Sec3/4 to end,W.P. ext (sig) → final rupture, Sec3/4 AE rise (4,565)		
70	↑CTC3290,H.T.	CTC3445↑3480	1st (global) = Sec2/3 AE peak (3530), 2nd = CTC3675	H.T. R.B. at ↓CTC3595 = σ_{in} (De↓),	CTC3480–3565, H.T. ext (sig,70°),	↓CTC3605, T.W., New V.W.P. (sub)-away-H.T.; CTC3605↑3640, all W.P. wid, W.S.-on-H.T.; CTC3640–3675 (2nd Abt phase), B-dots-on-H.T., CTC3675 = 2nd σ peak; CTC3675↑3750, σ_{in} (De↓) = W.S.»B-dots; CTC3750↓3810, Rock↓↓, W.S.-coa;
60	↑CTC2525,H.T.	CTC3215↑3315	CTC3315	H.T.R.B.at ↑CTC3405	CTC3315–3385, H.T. ext (sig),Inc-T.W., B-dots-on-H.T., Sec2/3 AE peak (3,370) = σ_{in} (Ac↓), CTC3385 = σ_{in} (De↓)	CTC2930↑3095 H.T.ext&wid; CTC3385↑3405 all W.P. wid, B-dot-mig-H.T.; CTC3405↓3430, lo-T.W.(sub), New P.W.P. (sub)-away-H.T.;CTC3430↑3440, T.W. and New P.W.P. wid (sig)CTC3440↓3460↑3480 (2nd Abt phase), B-dots↑, up-T.W.-con-New P.W.P., CTC3460 = σ_{in} (Ac↓) = W.S.»B-dots, CTC3460 = σ_{in} (De↓);CTC3480↓3490↑3495↓ 3515, W.S.-coa, Rock↓↓, T.W.R.B;
45	↓CTC2130T.W.(sub), H.T., A.W.	CTC2410↓2925, H.T. > flaw	1st (global) = CTC2985; 2nd = Sec4/5 AE rise (3830);	CTC2985–3045 (Abt phase), H.T. R.B. at CTC3045, Sec2/3 AE peak (3025) = σ_{in} (Ac↓), CTC3045 = σ_{in}(↓↑)		CTC3045↓3085, B-dots-on-H.T.;CTC3215↓3380, W.S.»B-dots, CTC3215 = σ↓(small);CTC3380↑3925, damaged zones appeared in corners, W.S.-coa, Rock↓↓, Sec4/5 AE rise (3830) = σ peak;CTC3925↓ 4055, cracks opened in macroscale, CTC4055 = Sec5/6 AE rise = σ_{in} (AC↓);CTC4055↑4110 (2nd Abt phase), W.S.s were fully opened from flaw to boundary, damaged zones were much developed; Sec6/7 AE peak (4,120) = σ_{in} (Ac↓);CTC4135↑4165, σ↓, distances between two surfaces of the open cracks increased slowly; CTC4165↓end, no dynamic rupture
30	T.W.(sub), H.T., A.W. appeared before the end of 2nd loading stage	CTC2695 = σ peak, H.T. > flaw, A.W. > flaw	1st = CTC2695; 2nd (global) = CTC3175; 3rd = CTC3620	CTC2805↑3070, A.W.R.B., A.W.&H.T. wid	CTC2695–2765, A.W. ext (sig), CTC2695 = σ_{in}(↑↓), CTC2765 = σ_{in}(↓↑)	CTC3070↓3110, B-dots-on-H.T.&A.W.; Sec4/5(3190)↑3275, B-dots↑ (sig)-mig-A.W. CTC3175 = 2nd σ peak; CTC3175-Sec4/5 (3190, 2nd Abt phase), σ↓ sharply; CTC3275↑3310, W.S.»B-dots; CTC3310↓3470, W.S.-coa & subsidiary

Table 4 *(continued)*

Inclination angle β	Inc-W.P.	σ peak	W.P. > flaw	1st R.B.	1st Abt phase	Other phenomena
						B-dots-on-A.W.; CTC3620 = 3rd σ peak, W.S.s were fully opened from flaw to boundary;CTC3620↑ 3680, σ↓ sharply, opened sections on two A.W. enlarged significantly, up-H.T.R.B.at ↑CTC3680;

Note. Inc-W.P. = incipient initiation of white patch; W.P. > flaw = the length of white patch exceeds the length of the preexisting flaw; 1st R.B. = first white patch reaches the specimen boundary; Abt phase = abrupt changing phase in crack-type ratio curves; ↑CTC3920 = shear crack ratio rises to the time of CTC3920; CTC3920↓4425 = from CTC3920 to CTC4425, the shear crack ratio declines; "=" = the time of two phenomena on the two sides of the equal are coincident; W.P. ext/wid (sig,70°) → final rupture = white patch extends/widens (significantly, at approximate 70° inclination) and led to the final rupture; Sec3/4 AE rise (4,565) = time section separation 3-4, the AE histogram begin to rise at (4,565 s); up/lo-T.W.(sub)/H.T./A.W. = the white patch of tensile wing (subtly)/horse tail/anti-wing appears at upper/lower part; σ_in (De/Ac↓/↑↓) = inflection point on the stress curve which is characterized as the start of (deceleration/acceleration of the overall stress decline trend)/or which is characterized as the point (where stress changes from rise to drop); New V/P.W.P.(sub)-away-H.T. = a new vertical/parallel white patch (subtly) appears at a distance away from the horse tail white patch; W.S.-on-H.T. = wrapped section appears on horse tail; B-dots (spa) -on/mig-H.T. = brightening dots (sparsely appears) are on/migrating along horse tail; W.S.»B-dots = wrapped sections replace brightening dots at the places of brightening dots; W.S.-coa = wrapped sections are coalescing; Rock↓↓ = rock material detaches from some severely wrapped sections; CTC3440↑3460↓3480 (2nd Abt phase) = the shear crack-type ratio rises from CTC3440 to CTC3460, and then declines from CTC3460 to CTC 3480, (characterized as the second abrupt phase with many fluctuations along the overall rising and declining trends); B-dots↑ = frequency of brightening dot appearance increases; up-T.W.-con-New P.W.P. = tensile wing white patch at the upper part connects to the new parallel white patch; σ↓(small) = a (small) stress drop.

CTC3215, while this phenomenon diminishes and is replaced by the phenomenon of wrapped section appearance after CTC3215. The physics of these two phenomena are different. However, without the aid of AE moment tensor analyses, these small changes in stress are most likely indiscernible.

Tracing back to the camcorder recordings at the time of the inflection points on stress curves (which are identified by the aid of mesoscale AE crack-type change points), the following two features are observed: (1) The plausible acceleration/deceleration transitions of the white patch extensions/widening are all coincident with some crack-type changing points in all five tests, and (2) some much subtle changes in the white patches, such as the appearance/disappearance of the brightening dots, the appearance of wrapped sections, and detachment of rock materials from the wrapped sections, are also coincident with some crack-type changing points in all five tests. These subtle changes will in most cases leave no trace on the stress curves and AE event histograms.

5.2. Cross Comparison Between Optical Observable Changes on Fracture Process and Mesoscale AE Crack-Type Changes

The correlation between the mesoscale AE shear crack inclination and the white patch extension/development possibly offers a new understanding on the white patch appearance and the fracture process. In previous literature, white patch is regarded as a direct optical phenomenon on the fracture process zone (Wong & Einstein, 2009b). The understanding on the mechanism of the microscale fracture accumulation in the white patch development process is limited. According to the present experimental results, white patches are obviously widened in shear crack rising periods for β = 90°, 70°, and 60° tests (the period from CTC4460 to the separation between time section 3 and time section 4 (AE rise at 4,565 s) for β = 90°; the length of white patch exceeds the length of preexisting flaw in the ratio-of-shear-crack-rising period from CTC3445 to CTC3480 for β = 70°; the length of white patch exceeds the length of preexisting flaw in the ratio-of-shear-crack-rising period from CTC3215 to CTC3315 for β = 60°). The new white patches formed in β = 70° and 60° tests also become obviously widened in shear crack rising periods.

1. For β = 70°, the new white patch incipiently initiates within the period from CTC3595 to CTC3605, where the ratio of shear crack first rises and then declines; the new white patch obviously develops within the period from CTC3605 to CTC3640, where the ratio of shear crack is in a rising trend.
2. For β = 60° test, new white patch incipiently initiates within the period from CTC3405 to CTC3430, where the ratio of shear crack is in a declining trend; the new white patch obviously develops within the period from CTC3430 to CTC3440, where the ratio of shear crack is in a rising trend.

These phenomena suggest that the widening of white patch may be accompanied by the increase of shear crack ratio in microscale. In previous literature, it is known that the propagation of shear crack may consist of multiple secondary cracks along its path (Petit & Barquins, 1988). The present experimental results provide further insights on the process of white patch development. Shear cracks will have more subsidiary cracks along their path, thus having wider process zone. The increase of shear crack components in microscale may lead to the macroscale white patch widening. For the new white patches that appeared in β = 70° and 60° tests, regardless of the inclination angles, the nature of these white patches is a combination of tensile cracks and shear cracks in the microscale.
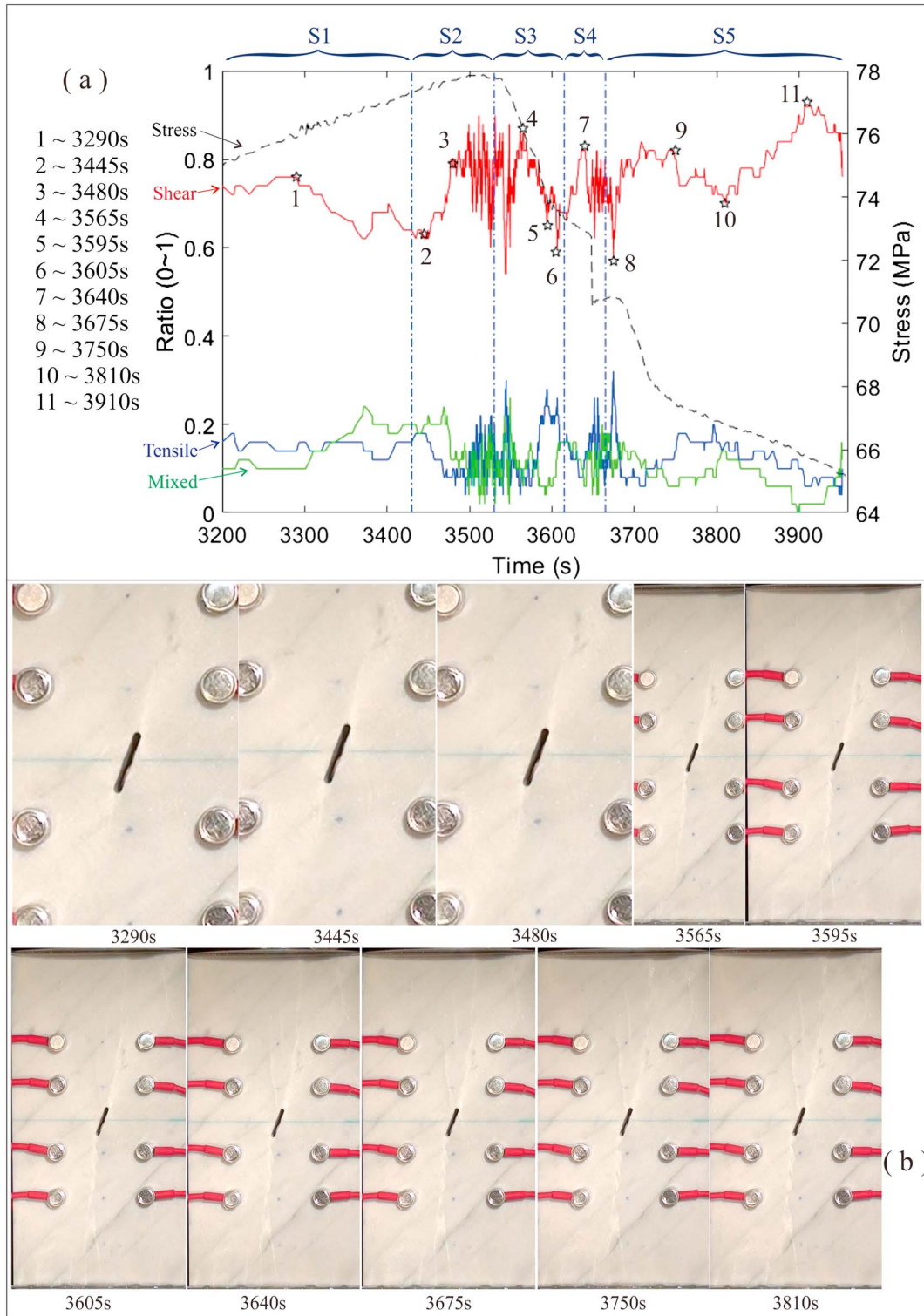
Figure 17. β = 70°. (a) Stress and acoustic emission (AE) crack-type ratio plot (only plotted from 3,200 s to end of the test). Changing points of AE crack-type ratios are labeled as 1–11 in the plot. The *i*th time sections (in Table 3), which are separated by vertical dashed-dotted lines, are labeled as S_i (blue letters) at the top of the plot. (b) Camcorder screenshot (enlarged as necessary) at AE crack-type changing points (labeled with its time of occurrence; color online).

Figure 18. β = 90° (a) Stress and acoustic emission (AE) crack-type ratio plot (only plotted from 3,000 s to end of the test). Changing points of AE crack-type ratios are labeled as 1–3 in the plot. The *i*th time sections (in Table 3), which are separated by vertical dashed-dotted lines, are labeled as S_i (blue letters) at the top of the plot. (b) Camcorder screenshot (enlarged as necessary) at AE crack-type changing points (labeled with its time of occurrence; color online).
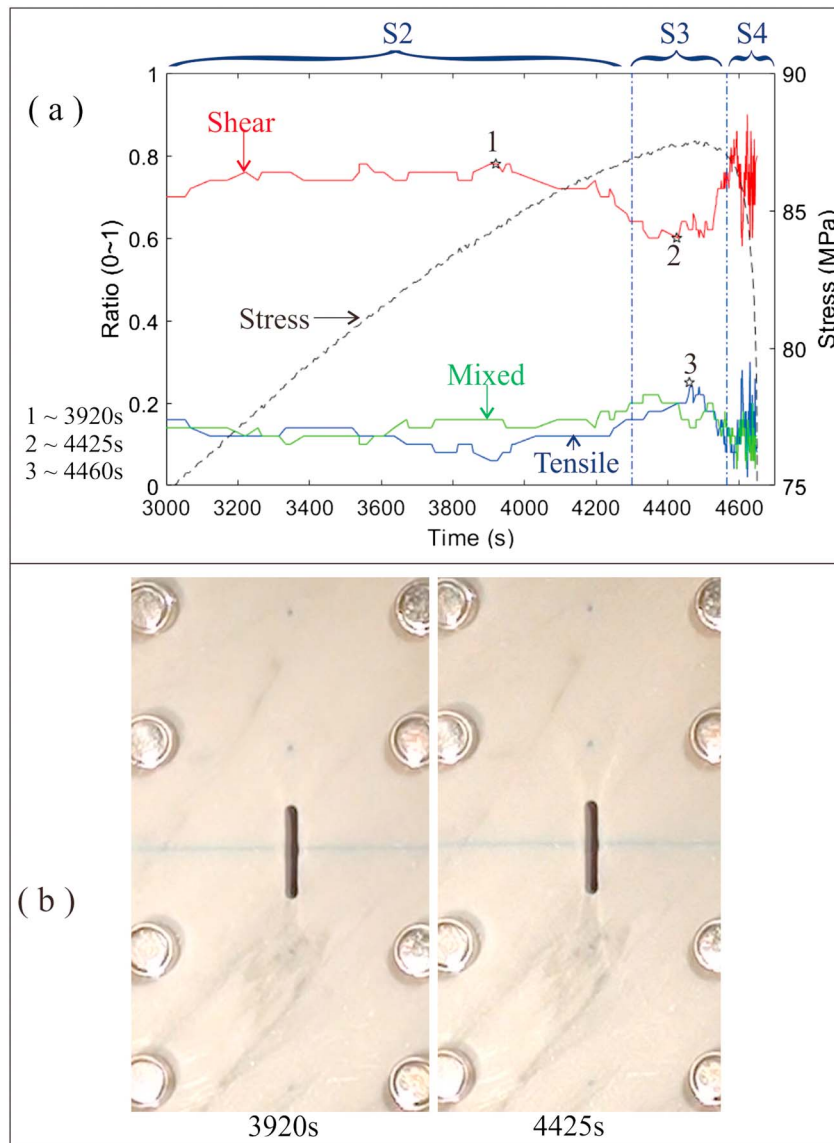
For β = 45° and 30° tests, the white patch becomes longer than the preexisting flaw within the periods when the shear crack ratio declines (from CTC2410 to CTC2925 for β = 45° test and from CTC2130 to CTC2695 for β = 30° test). However, the camcorder recording of these two tests reveals that, for β = 45° test, the horse tail propagation direction has curved toward the vertical from CTC2410 to CTC2925, and for β = 30° test, the dominant fracture propagation is antiwing white patches, whose macroscale cracking is interpreted as tensile. These two phenomena show the agreement between macroscale optical observation and the microscale AE moment tensor interpretation.

For β = 45° test, the agreement on microscale moment tensor interpretation and macroscale phenomena is also observed after the cracks become fully opened. In that test, from CTC4135 to CTC4165, the distances between two surfaces of the open cracks increase slowly, while the ratio of microscale shear crack rises in that period. The stress drop in that period is much slower than that in its previous period. This phenomenon can
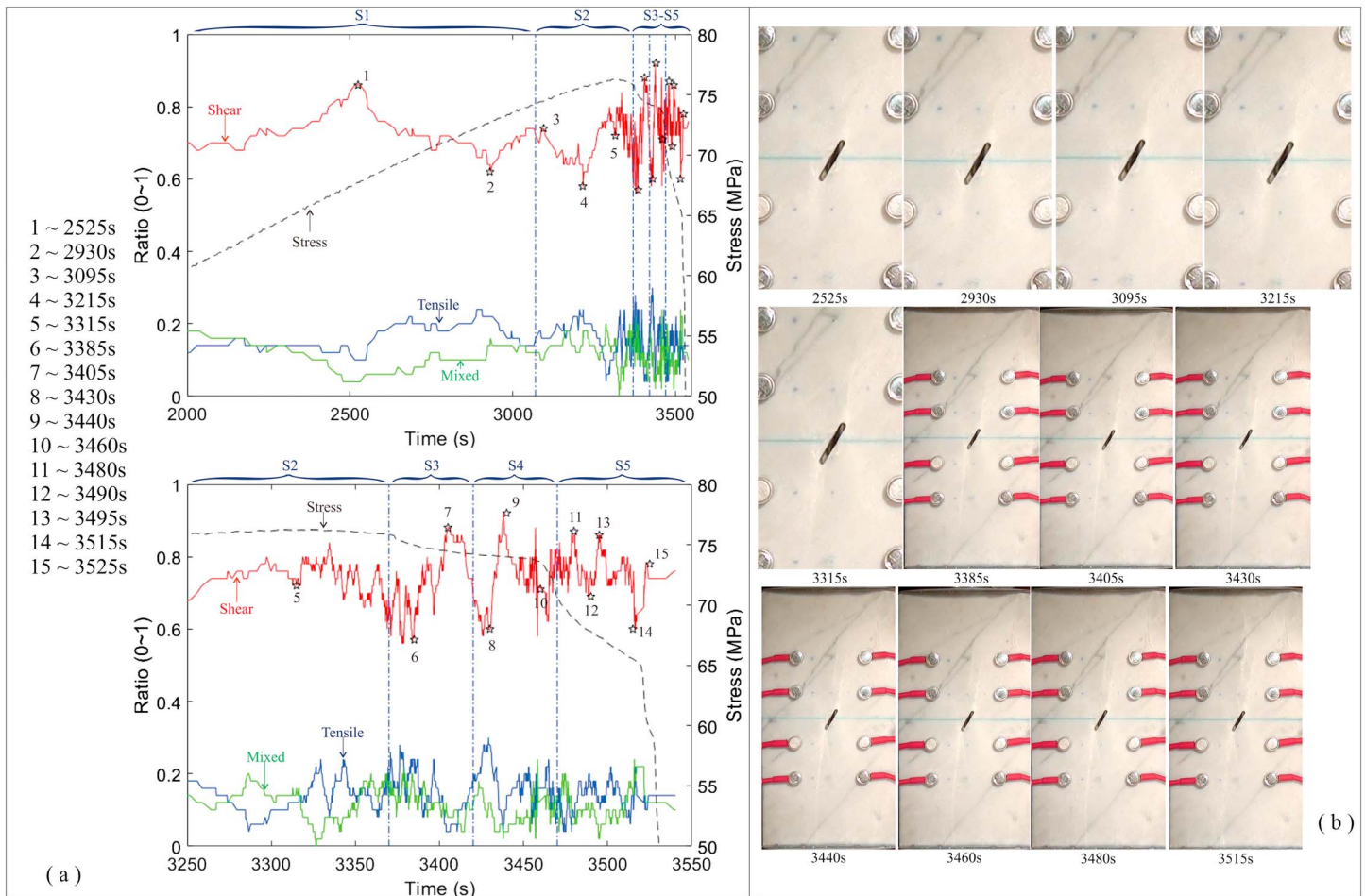
Figure 19. β = 60° (a) Stress and acoustic emission (AE) crack-type ratio plot (only plotted from 2,000 s to end of the test for the top plot and from 3,250 s to end of the test for the bottom enlarged plot). Changing points of AE crack-type ratios are labeled as 1–15 in the plots. The *i*th time sections (in Table 3), which are separated by vertical dashed-dotted lines, are labeled as S_i (blue letters) at the top of each plot. (b) Camcorder screenshot (enlarged as necessary) at AE crack-type changing points (labeled with its time of occurrence; color online).

be explained by the following reason. As the macroscale crack opens, the specimen is split into two major rock columns supporting the axial loading individually. The ratio of microscale shear crack will rise within these two rock columns instead of the tensile opening along the opened macroscale tensile crack.

In contrast with the previous macroscale interpretations based on the high-speed video examination (Wong & Einstein, 2009a), which classified a crack into shear or tensile mostly by observing its rupture dynamics, the microscale interpretation suggests the existence of both microscale shear and tensile components during the formation of a macroscale crack. However, the microscale tensile components are in rising trends during the crack formation which are interpreted as tensile in macroscale. Meanwhile, for the cracks which are interpreted as mixed mode or shear in macroscale, the microscale shear components are in rising trends during the crack formation.

One interesting issue is that the SiGMA moment tensor inversion has also been applied in concrete tests (Ohtsu & Tomoda, 2007) for identifying the different mesoscale crack mechanisms. For concrete, different crack mechanisms can also be identified by AE parametric analysis (Aggelis, 2011). According to Ohtsu and Tomoda (2007), the macrocrack in concrete is also found to consist of different mesoscale crack components, and Ohtsu and Tomoda (2007) attribute the cause of different mesoscale crack components to the zigzag cracking path. However, one must notice that the physics of the different crack mechanisms in concrete is distinctively different from those in rocks.
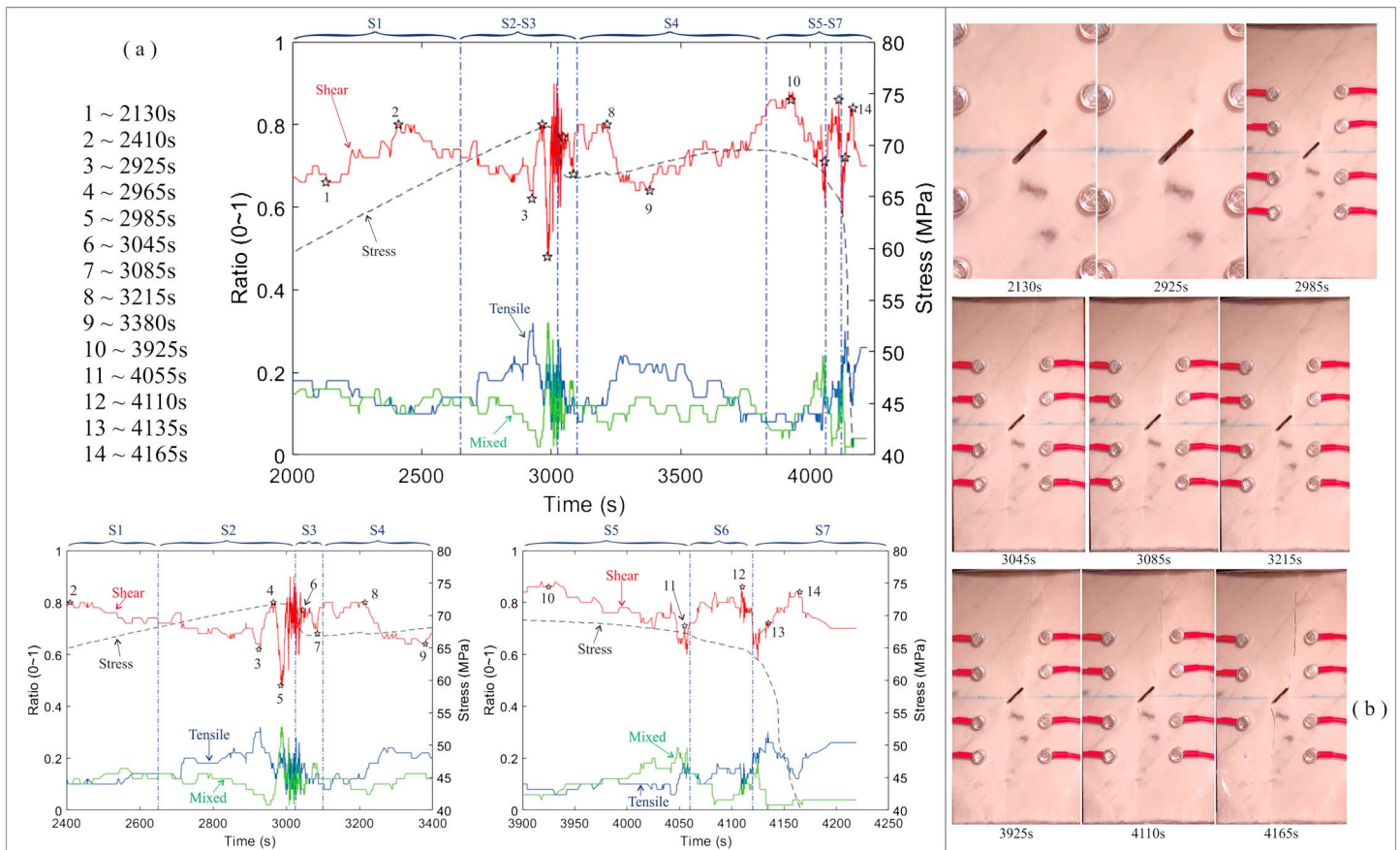
Figure 20. β = 45° (a) Stress and acoustic emission (AE) crack-type ratio plot (only plotted from 2,000 s to the end of the test for the top plot and from 2,400 to 3,400 s of the test for the bottom left enlarged plot and from 3,900 s to the end of the test for the bottom right enlarged plot). Changing points of AE crack-type ratios are labeled as 1–14 in the plots. The *i*th time sections (in Table 3), which are separated by vertical dashed-dotted lines, are labeled as S_i (blue letters) at the top of each plot. (b) Camcorder screenshot (enlarged as necessary) at AE crack-type changing points (labeled with its time of occurrence; color online).

5.3. New Phenomena Observed Under the Aid of Multiscale Comparison

The brightening dots and wrapped sections begin to appear after the first stress drop, and the white patches have reached the specimen boundary (the period from CTC3315 to CTC3385 of β = 60° test is the only exception, while even for that test, the frequency of brightening dots' appearance after the white patch has reached the specimen boundary is obviously higher than the frequency of brightening dots appearance before the white patch reaches boundary), where the AE event activities remain active. The transition times from solely white patch extension to the appearance of these phenomena along the formed white patches/cracks are coincident with certain crack-type changes. This correlation suggests new stages in the fracture process. Previous literature seldom reports the phenomenon of brightening dots. We believe a necessary condition for the appearance of such local brightening grain is the large displacement along the two fracture surfaces. Under this condition, mineral grains will be greatly crushed, thus enhancing grain splitting. Some reflective granular facets will be exposed toward the observer (camcorder), which gives a shiny appearance in the loading process. This phenomenon suggests a transition of the physics within the fracture process zone. Literature of loading tests in Carrara marble (Cheng, 2015; Cheng et al., 2016) reported that the intergranular cracks (grain debounding along grain boundaries) dominate at early loading stages, while the percentage of transgranular cracks rises only at later loading stages. It is reasonable to suggest that the thin white patch extension is primarily dominated by grain debounding. Meanwhile, as the displacement along two fracture surfaces reaches a sufficiently high level, granular crushing will replace the grain debonding as the dominant mechanism for fracture process. Later, in all tests, the wrapped sections occur along the white patch (fracture process zone) after the appearance of brightening dots. It also suggests a transition
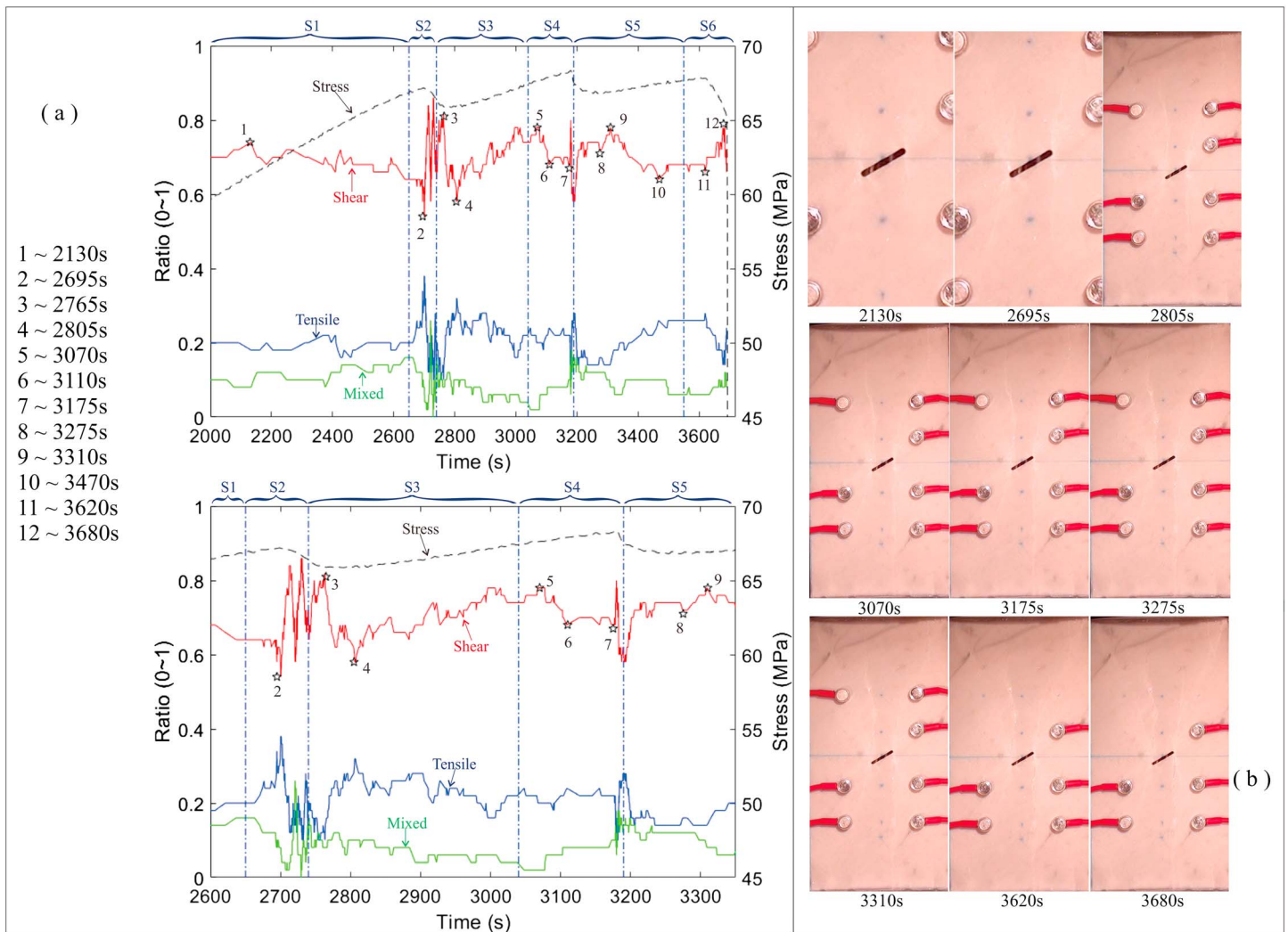
Figure 21. β = 30° (a) Stress and acoustic emission (AE) crack-type ratios plot (only plotted from 2,000 s to the end of the test for the top plot and from 2,600 to 3,350 s of the test for the bottom enlarged plot). Changing points of AE crack-type ratios are labeled as 1–12 in the plots. The *i*th time sections (in Table 3), which are separated by vertical dashed-dotted lines, are labeled as S_i (blue letters) at the top of each plot. (b) Camcorder screenshot (enlarged as necessary) at AE crack-type changing points (labeled with its time of occurrence; color online).

of grain crushing to a larger scale cracking process, which is characterized by the rock fragment detachment from the white patch/crack paths.

5.4. New Understanding on the Role of Stress Drop (Stress Release) Period in the Development of Fracture Process Zone

The AE source location and moment tensor inversion technique have been successfully used earlier to characterize the extension of fracture process zones (Carvalho & Labuz, 2002; Li & Einstein, 2017; Zang et al., 1998; Zang et al., 2000; Zietlow & Labuz, 1998). The present experimental observation combining optical observation and AE moment tensor interpretation suggests that, besides the forward fracture propagation, much more complex fracture processes may continue to operate within the fracture process zones.

The majorities of the AE events in the clusters of different tests (also corresponding to the peaks in AE event histograms) occur in the stress drop periods (labeled as section *i-j* in Figures 17a, 18a, 19a, 20a, and 21a). In these periods, substantial observable extension/widening of the white patches occur. This phenomenon manifests the continual development of fracture process zone in the stress drop period, whereas previous

research may have failed to observe this once the applied force was designed to be monotonically increasing in their loading procedure or a very high displacement rate was designed. This phenomenon also further evidences the existence of the critical thresholds for the crack coalescence at the subscales. Similar threshold concepts had been reported earlier literature. For intact rock core sample, there was a threshold between stable/unstable microcrack growth (Hoek & Martin, 2014). For the fracture coalescence test, thresholds between stable microcrack growth, microcrack coalescence, and macrocrack initiation were proposed by Moradian et al. (2015). These two kinds of thresholds (for intact rock core or for specimens containing double preexisting flaws) were both suggested based on the identification of the change of AE hit rate or the combination of changes in AE hit rate and energy release rate. Additionally, in the present study, the stress drops and the white patch extensions are closely accompanied by the changes in crack-type ratio curves. This phenomenon suggests that the changes in crack-type ratio curves may also be useful for identifying these subscale thresholds. In addition, the certain crack-type changes before stress drops are also influenced by the β angle.

5.5. Implication of Limitations on AE Source Location Analysis

Comparing the camcorder video recordings with the AE source location results, the first white patch is observed to develop well before the appearance of any AE clusters. The only exception is β = 30° test, where a small cluster of AE sources occurs when the first white patch appears. This phenomenon supports the speculation that some microscale cracking events have not been picked up by the AE array. The AE clusters and white patch paths match closely before the white patches reach the specimen boundaries in all five tests (Figures 7–11). These matching gradually disappear after the first white patches reach the specimen boundaries and become open. Afterward, the AE source location becomes scattered. It is expectable that after the major cracks have developed, the microscale crack development may migrate to the remaining parts of the specimens as these parts will be under greater stress after the first white patches/cracks have developed. Another possible explanation to this scattered AE source location may be the influences of the fracture formation and opening on the accuracy of AE source locations. This speculation is coincident with the fact that the initial error estimations reported in research on intact samples used to be smaller than that of research on preflawed samples. Generally, larger initial error estimations for specimens containing preexisting natural fault (Thompson et al., 2009) and saw-cut fault (McLaskey et al., 2014) were made as compared with those (initial error estimation) for intact rock specimens (Graham et al., 2010; Lockner et al., 1991; Stanchits et al., 2009; Zang et al., 1998; Zang et al., 2000). In the intact rock specimens, error estimations smaller than 3 mm could be achieved, while much larger error estimations were expected for the tests on specimens containing natural/saw-cut preexisting flaws.

5.6. Issues on the Selection of Mesoscale AE Crack-Type Thresholds

The presently adopted AE crack-type classification thresholds are, $\frac{X}{X+Y+Z} > 0.6$ for shear crack, $0.4 < \frac{X}{X+Y+Z} < 0.6$ for mixed mode crack, and $\frac{X}{X+Y+Z} < 0.4$ for tensile crack. The selection of the thresholds in classifying the crack types is subjective to some extent. For instance, Charalampidou et al. (2014) discussed the influence of shifting the thresholds. Different values of thresholds were also proposed by Ohtsu (1991, 1995). However, because the ratios of mixed mode cracks are comparatively small, the influence of shifting the thresholds will not be significant. Moreover, different selections will not affect the time of the changing points on the crack-type ratio curves. In the initial loading stages, the crack-type ratio curves are perturbed much greater than in the following stages. This may be attributed to two reasons. First, the different loading rates will have influenced the source feature at the initial loading stages. Second, the small AE event numbers in initial stages exaggerate the random perturbation effect. However, the in-depth investigation of loading rate influence is out of the scope of the present paper.

5.7. Moment-Frequency Distribution of Relative AE Moment

Among the results of relative AE moment-frequency distributions, the distribution appears to satisfy a log-log relationship. This is understandable under the rationale of Gutenberg-Richter (G-R) law considering that the moment can be converted into moment magnitude by $\frac{2}{3} \left[\log_{10} M_{AE} - C \right]$, where C is a constant which does not affect the shape of curves if one considers that the M_{AE} are relative values.

Kwiatek et al. (2014) used a different method to calculate the moment magnitude for the laboratory scale obtained AE moments. In their calculation, the AE moment magnitude was calculated as

$$M_{AE} = \log_{10}\left(\frac{1}{n}\sum_{i=1}^{n}(A_iR_i)^2\right)^{0.5}$$

where A_i and R_i were the first P wave amplitudes and source to sensor distances.

Since in the present study, the AE moment-frequency displays a linear relationship in the log-log coordinate, and both the calculation of the present study and the above equation are based on the first P wave amplitude, the result of the above calculation would also likely produce a suitable AE moment magnitude-frequency relationship under the rationale of the G-R law. Other estimations of the AE moment magnitude also exist, for instance, in Zang et al. (1998),

$$M_{AE} = \log_{10}\left(\frac{1}{n}\sum_{i=1}^{n}\left(A_{i\,max}\frac{R_i}{10}\right)^2\right)^{0.5}$$

The above was used for estimating the amplitude of focal magnitude. To the best of the authors' knowledge, there is no decisive conclusion of which calculation gives the best estimation. Some researchers checked the open source seismic data by statistical methods (Costa et al., 2016; Tsai et al., 2015) and argued that the favor of simplicity of the G-R law may suffer the problem of information loss and the Zipf-Mandelbrot distribution may potentially be a better summary for the earthquake magnitude-frequency distribution.

The truncations or turning angles of the relative AE moment-frequency curves may be attributed to two factors. First, in the small AE moment domain, some microscale AE cannot be registered by the system. In Cheng's (2015) observation of granular scale microcracks on specimens containing en-echelon flaws, the results were presented in terms of microcrack densities of shear stress zone and tensile stress zone. In the present study, the crack-type ratio for 0% to 90% stress range is not comparable with Cheng's (2015) microcrack densities in shear stress zone and tensile stress zone. Although the tests of Cheng (2015) were also conducted in prismatic Carrara marble specimens, the expected similarity between the ratios of AE microcrack types and the microcrack densities in the shear stress zone and tensile stress zone under fluorescent dye observation is not observed. Second, for the large AE moment domain, as the microscale-mesoscale fractures are scaled up by coalescing and connecting neighboring fractures, the scale of the source may become comparable with the scale of the source-to-sensor paths. This fact undermines the theoretical foundation of laboratory scale AE source location and moment tensor inversion. Therefore, at both the ultrasmall and ultralarge domains, the relative AE moment-frequency curves always have turning/truncated points in the log-log plots.

Many questions still remain unanswered in the laboratory scale observed relative AE moments. The above-mentioned factors suggest the necessity of further research and discussion on the laboratory scale AE activities regarding the G-R law. However, a thorough discussion of this issue exceeds the scope of the present paper.

6. Conclusions

This paper presents a method of multiscale multisystem observation and interpretation on the fracture process on specimens containing a single preexisting flaw. The results manifest its capability to reveal the new phenomena in the fracture process of uniaxial compression tests on specimens containing a single flaw. Comparing with the previous research, the major discoveries and new understanding on the fracture process on specimens containing a single preexisting flaw can be summarized as follows:

1. In the aspect of mechanical analysis, in addition to the major stress drops, the proposed method successfully identifies the subtle stress perturbations and inflection points on stress curves through the aid of coincident substantial mesoscale AE crack-type ratio change. These subtle changes used to be neglected if without the aid of subscale AE crack-type information.

2. The correlation between macroscale-mesoscale interpretations on the crack type can be summarized in two aspects. In β = 90°, 70°, and 60° tests, the prominent widening and extension of the white patches occur in the mesoscale AE shear crack rising period; in β = 45° and 30° tests, the prominent extension of the white patches occurs in the mesoscale AE shear crack declining period. In macroscale, the cracks of β = 90°, 70°, and 60° tests are shear or mixed mode; the cracks in β = 45° and 30° tests are tensile. In mesoscale, shear, tensile, and mixed-mode cracks are all present in the development process of fractures regardless if these fractures are interpreted as shear, tensile, or mixed mode in macroscale. However, the microscale tensile components are in rising trends during the formation of macrocracks which are interpreted as tensile in macroscale. Meanwhile, for the cracks which are interpreted as mixed mode or shear in macroscale, the microscale shear components are in rising trends in the formation of such cracks.

3. The coincidence of certain mesoscale AE crack-type changes and the phenomena of brightening dot migration and the subsequent appearance of wrapped sections appear to be new stages, which should be included in the fracture process. However, as they occur in the domain after the first stress drop, they are not easily picked up in previous research.

4. According to the AE histograms on the stress drop period, the stress drop period may play a more important role in the fracture process as compared with previous understanding. In previous studies on the fracture process of specimens containing a single preexisting flaw, this continual development of fracture process zone in the stress drop period, whereas previous research may have failed to observe this once the applied force was designed to be monotonically increasing in their loading procedure or a very high displacement rate was designed.

5. The scattering of AE source locations after the first white patches have reached the specimen boundary suggests a shift of stress concentration to the remaining parts of the specimens after the white patches have reached the specimen boundary. Meanwhile, such scattering may also be attributed to the recently formed fracture which affects the accuracy of source location.

6. The moment-frequency distribution of the AE moment obtained in the present study displays a log-log relationship, which is understandable under the rationale of G-R law considering that the moment can be converted into moment magnitude by $\frac{2}{3}\left[\log_{10} M_{AE} - C\right]$.

Appendix A
A1. White Patch, Brightening Dots, and Wrapped Sections

White patch refers to the development of whitish phenomenon associated with the fracture process zone on the specimen surface. This term has been thoroughly used in previous research focusing on the fracture process in Carrara marble specimens (i.e., Bruno & da Silva, 2016; Cheng et al., 2015; Cheng et al., 2016; Cheng & Wong, 2018; Moradian et al., 2015; Wong & Einstein, 2009a, 2009b). According to the microobservation (SEM; Wong & Einstein, 2009b), the white patches are associated with the extensive development of microcracks in the fracture process zone. An example of this whitish phenomenon is shown in Figure A1a.

The phenomena of brightening dots and wrapped section are illustrated in Figures A1b and A1c, respectively. In Figure A1b, several large brightening dots that appeared along the white patches (fracture process zones) are indicated by the red arrows. In the later fracture process, more brightening dots will appear along the fractures. The brightening dots at some places will disappear, while almost at the same time, new brightening dots will appear at other places. The brightening dots thus appear to migrate along the fractures. In Figure A1c, the red ellipse encloses a wrapped section which has partially opened. The two lower green circles enclose two sections with severe tortuosity. In the later fracture process, the fracture sections at these two places will conspicuously wrap inward or outward. This tortuosity may be related to some higher level of stress concentration as the open sections of the fracture in most of time first appear at these locations. As the fracture process continues, the wrapped sections spread out along the fractures, connecting to each other one by one, and finally forming a continuous open macroscale fracture.

A2. Parameters Provided by PAC for Picking AE Waveforms

The present data acquisition setup is hit-based streaming. The continuous-based streaming is not selected because it is uneconomical for the present experimental test. For the hit-based streaming, a waveform can be recorded according to parameters of threshold, HDT, and HLT (see section 2.2). The operating
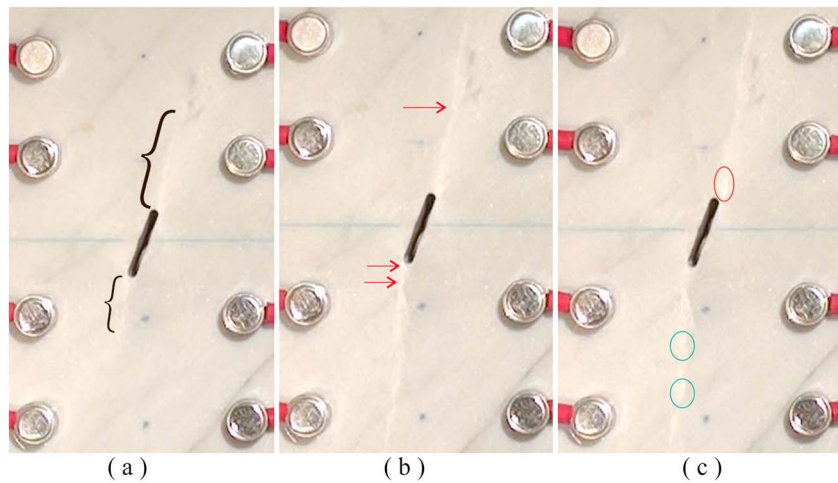
Figure A1. Illustration of (a) white patch, (b) brightening dots, and (c) wrapped sections.

principle is shown in Figure A2. A waveform will be separately recorded once the following conditions are satisfied, (1) it crosses the threshold, (2) it has a time at its prethreshold-crossing section that is without any threshold-crossing and longer than the HDT, and (3) its time gap between the first threshold-crossing and the end of the previous waveform in the same channel is larger than the HLT.

The floating type threshold means that when the signal level is higher than the threshold, the threshold will shift to the value of initial threshold plus floating value (Physical Acoustic Corporation, 2001). Here a 5-dB floating value has been used.

A3. Calibration Procedures and Calibration Results

The present calibration method is based on the evaluation of the sources for relative calibration focused on the first peak amplitudes in Xiong and Wong (2017). It is conducted in two steps. In the first step, a PICO sensor (its aperture is smaller than that of NANO-30 for better calibration) manufactured by PAC with 200–
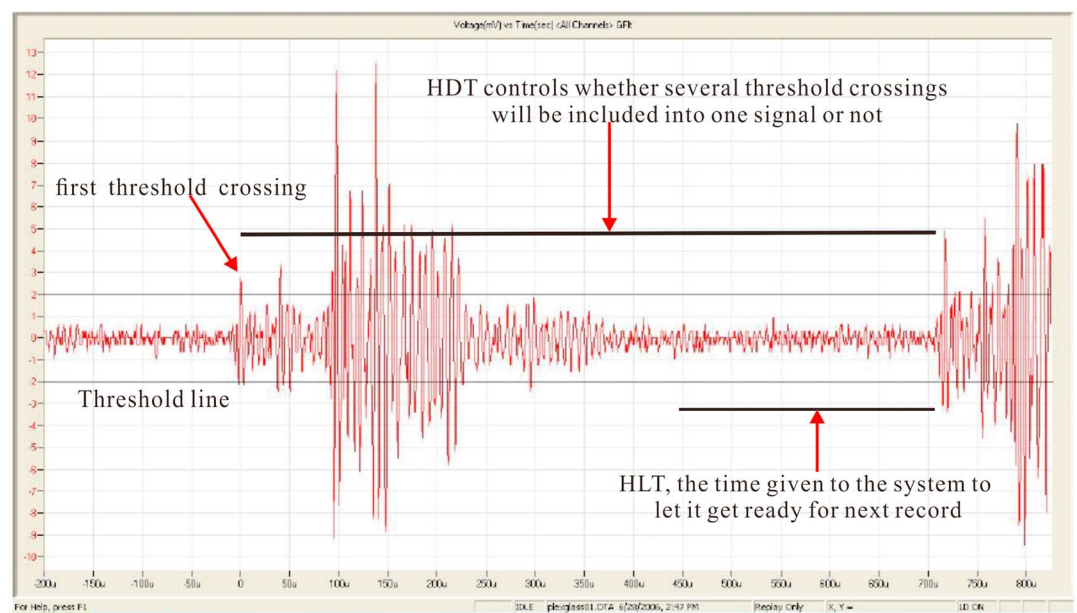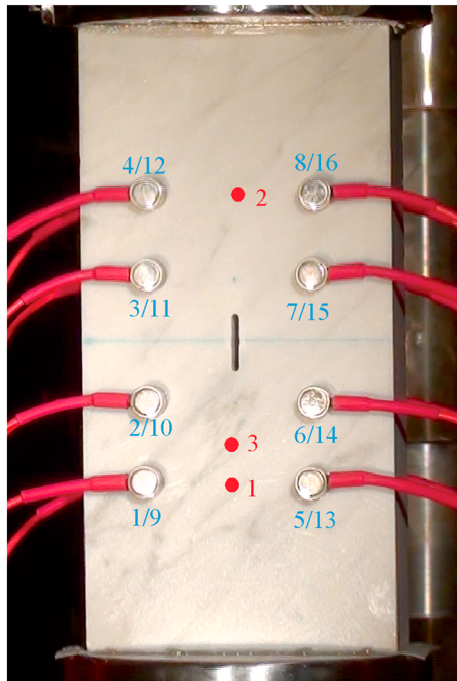

Figure A2. Illustration of the acoustic emission data acquisition parameters, edited after Physical Acoustic Corporation manual (Physical Acoustic Corporation, 2001).

i/j sensor numbers for front/back sides
k number for dots of energized
PICO sensor source

Figure A3. Illustration for calibration process.

750 kHz operating frequency and 550-kHz resonant frequency in V/μbar unit is used to transmit elastic waves at the fixed points (red dots in Figure A3). These points are designed in a way such that the signal-to-sensor paths for several pairs of sensors with identical distance, and incident/takeoff angles can be produced. Assuming that all the sensors can only have normal direction movement and response, the directionality of the PICO sensor can be negligible. Therefore, the PICO sensor will generate an elastic wave with planar-isotropic amplitude. When the PICO sensor is energized, a single polar rectangular pulse of 125 V and 1.0-μs duration is given to the sensor. The selection of the pulse duration is to maximize the sensor's vibration according to the reported sensor's resonant frequency in the PAC manual of PICO sensor (Physical Acoustic Corporation, 2011b). Based on the coordinates and the normal directions of the sensors, the elastic waves from points 1, 2, and 3 and combination of 1 and 3 are used to calibrate the sensor pairs of 1:2:5:6, 3:7, 4:8, 9:10:13:14, 11:15, and 12:16, respectively.

In the second step, sensors 1 to 16 are energized sequentially by a single polar rectangular pulse of 125 V and 1.7-μs duration. The selection of the pulse duration is to maximize the sensor's vibration according to the reported sensor's resonant frequency based on the PAC manual of Nano-30 sensor (Physical Acoustic Corporation, 2011a). When one particular sensor is energized, the remaining 15 sensors will be triggered by the elastic wave transmitted by that energized sensor. The network sensor calibration method (Davi et al., 2013) is used to extract the relative site-effect values of the sensors. In this method, an empirical equation is used to describe the relation between the received AE amplitude and the energized PZT sensor source.

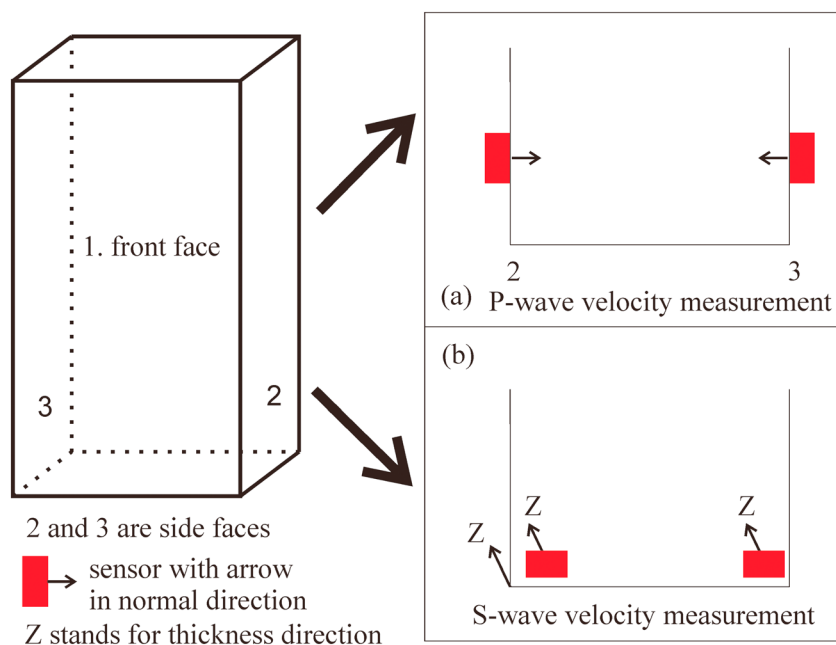$$A_{ij} = \frac{1}{r} \exp\left(-a\alpha^b\beta^b\right) S_i S_j \tag{A1}$$

Figure A4. Measurement of (a) *P* wave and (b) *S* wave velocity.

Table A1
Calibration Results for All Tests

| Flaw angle (β) S_i (Cs)	Close to 90	70	60	45	30
1	0.9195	1.2159	1.1246	0.5272	1.1378
2	0.4589	1.2280	1.0394	1.2099	1.1959
3	0.5357	1.4031	1.2227	1.1616	1.2635
4	1.0544	1.2831	1.1576	0.9835	1.1154
5	1.0735	1.2072	1.3118	1.3661	0.7431
6	0.9895	0.6605	1.0635	1.3166	1.3197
7	1.0863	1.1222	1.1175	1.2859	1.1741
8	0.9099	1.0973	1.1375	1.1346	1.1938
9	1.0823	1.2917	1.1162	1.1940	1.1827
10	0.8984	1.1237	0.9768	1.0030	1.2397
11	1.0545	1.1851	0.7693	0.8931	1.2021
12	0.9797	1.1450	0.6307	1.0707	1.2690
13	0.9291	0.8256	1.1932	1.0508	0.7905
14	1.0526	1.2767	1.0806	0.9899	1.2491
15	0.9495	1.1118	0.7763	1.2081	1.2428
16	0.9442	1.1757	0.8224	1.0248	1.2768

where A_{ij} is the resulted sensor output when sensors i and j play as transmitting and receiving sensors, respectively; r is the distance between sensor i and j; α and β are the incidence and takeoff angles of the transmitting and receiving sensors; S_i and S_j are the coefficients of the local effect (site effect); a and b are constants in this model.

Because of the presence of a preexisting flaw, the number of sensor pairs that can be input into equation (A1) is greatly reduced. However, with the relative value obtained from step 1, the overdetermined condition of the sensor network will be greatly increased. Therefore, based on the sensors' coordinates and normal directions information, the received signal is sufficient to calibrate all 16 sensors used in the test.

Based on the signal received from step 1, a source location is conducted. From that source location result, the distance from the PICO sensor's center point to the located source point is 4.2 mm in average. The average distance from the PICO sensor's center to the located source point in the thickness direction is 1.9 mm. Notice that the source provided by the PICO sensor itself has 5-mm aperture. This error suggests that the performance of the AE sensor array is quite satisfactory.

A4. *P* Wave and *S* Wave Velocity

The measurement of the *P* wave velocity and *S* wave velocity is conducted by the PROCEQ ultrasonic tester and two PICO sensors on the rock specimen before the loading test. When the *P* wave measurement is conducted, the two PICO sensors are attached onto the side faces depicted in Figure A4a. Multiple single dipole rectangular pulses with 1.0-μs duration are given to one of the two sensors. The other sensor will receive the
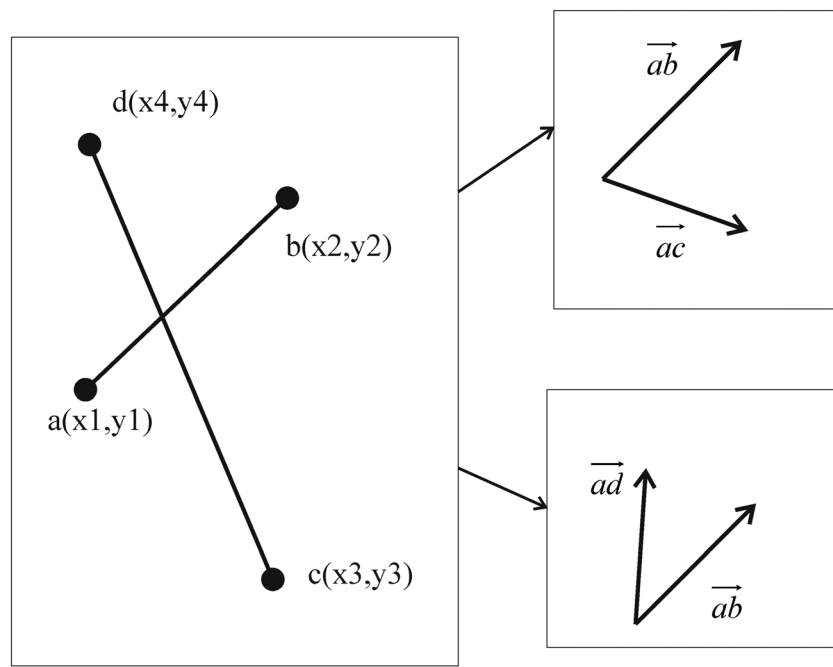
The cross product of $\vec{ab}$ and $\vec{ac}$ is negative, while the cross product of $\vec{ab}$ and $\vec{ad}$ is positive. So the product of these two cross products is negative.

Figure A5. Illustration of the logic algorithm on judging whether the source-to-sensor path is intercepted by the preexisting flaw or not.

signal from that energized sensor. As the primary vibration direction of PICO sensor is the normal direction of the sensor, this arrangement maximizes the *P* wave transmission and receiving.

When *S* wave measurement is conducted, the two PICO sensors are attached onto the front face as depicted in Figure A4b. Again, multiple single dipole rectangular pulses with 1.0-μs duration are given to one of the two sensors. The other sensor will receive the signal from that energized sensor. This arrangement maximizes the *S* wave transmission and receiving.

Before each measurement, the time difference reported between the wave transmission sensor and the receiver is calibrated by a standard manufactured polymer core provided by PROCEQ. As the length and the wave velocity of the polymer core are known, any error on the electric system in reporting the time difference between the transmitter and the receiver can be calibrated before the *P* wave and *S* wave velocity measurements.

A5. Calibration Results of the Tests

The calibration results for all tests are listed in the Table A1 algorithm on judging whether the source-to-sensor path was intercepted by the preexisting flaw or not.

The source-to-sensor path and the open preexisting flaw can be viewed as two sections on X-Y plane (because the preexisting flaws cut through the specimens' thickness). Assume the source-to-sensor path is section "$\overline{ab}$" and the open preexisting flaw is section "$\overline{cd}$." As Figure A5 illustrates, mathematically, for a point in the left-hand side of a vector, the cross product of these two vectors $(\overrightarrow{ab} \times \overrightarrow{ad})$ shall be positive; for a point in the right-hand side of a vector, the cross product of these two vectors $(\overrightarrow{ab} \times \overrightarrow{ac})$ shall be negative. If one section is intercepted by the other section, the two points of this section shall be on two sides (left-hand side and right-hand side) of the other section. Therefore, to judge whether the two sections are intersected or not, we have

$$\begin{cases} \text{crossproduct}\left(\overrightarrow{ab}, \overrightarrow{ac}\right) \times \text{crossproduct}\left(\overrightarrow{ab}, \overrightarrow{ad}\right) < 0 \\ \text{crossproduct}\left(\overrightarrow{cd}, \overrightarrow{ca}\right) \times \text{crossproduct}\left(\overrightarrow{cd}, \overrightarrow{cb}\right) < 0 \end{cases}$$

References

Aggelis, D. G. (2011). Classification of cracking mode in concrete by acoustic emission parameters. *Mechanics Research Communications*, *38*(3), 153–157. https://doi.org/10.1016/j.mechrescom.2011.03.007

Alber, M., & Hauptfleisch, U. (1999). Generation and visualization of microfractures in Carrara marble for estimating fracture toughness, fracture shear and fracture normal stiffness. *International Journal of Rock Mechanics and Mining Sciences*, *36*(8), 1065–1071. https://doi.org/10.1016/S1365-1609(99)00069-6

Bruno, M. G., & da Silva, G. (2016). *Fracturing processes and induced seismicity due to the hydraulic fracturing of rocks*, (Doctoral of Philosophy). Massachusetts Institute of Technology.

Carpinteri, A., Xu, J., Lacidogna, G., & Manuello, A. (2012). Reliable onset time determination and source location of acoustic emissions in concrete structures. *Cement and Concrete Composites*, *34*(4), 529–537. https://doi.org/10.1016/j.cemconcomp.2011.11.013

Carvalho, F. C. S., & Labuz, J. F. (2002). Moment tensors of acoustic emissions in shear faulting under plane-strain compression. *Tectonophysics*, *356*(1-3), 199–211. https://doi.org/10.1016/S0040-1951(02)00385-2

Charalampidou, E.-M., Stanchits, S., Kwiatek, G., & Dresen, G. (2014). Brittle failure and fracture reactivation in sandstone by fluid injection. *European Journal of Environmental and Civil Engineering*, *19*(5), 564–579. https://doi.org/10.1080/19648189.2014.896752

Cheng, Y. (2015). *Studies on the formation of faults from en-echelon fractures in Carrara marble*, (Doctoral of Pshilosophy). Nanyang Technological University.

Cheng, Y., & Wong, L. N. Y. (2018). Microscopic characterization of tensile and shear fracturing in progressive failure in marble. *Journal of Geophysical Research: Solid Earth*, *123*, 204–225. https://doi.org/10.1002/2017jb014581

Cheng, Y., Wong, L. N. Y., & Maruvanchery, V. (2016). Transgranular crack nucleation in Carrara marble of brittle failure. *Rock Mechanics and Rock Engineering*, *49*(8), 3069–3082. https://doi.org/10.1007/s00603-016-0976-2

Cheng, Y., Wong, L. N. Y., & Zou, C. J. (2015). Experimental study on the formation of faults from en-echelon fractures in Carrara marble. *Engineering Geology*, *195*, 312–326. https://doi.org/10.1016/j.enggeo.2015.06.004

Costa, L. S., Lenzi, E. K., Mendes, R. S., & Ribeiro, H. V. (2016). Extensive characterization of seismic laws in acoustic emissions of crumpled plastic sheets. *EPL (Europhysics Letters)*, *114*(5), 59002. https://doi.org/10.1209/0295-5075/114/59002

Davi, R., Vavryčuk, V., Charalampidou, E.-M., & Kwiatek, G. (2013). Network sensor calibration for retrieving accurate moment tensors of acoustic emissions. *International Journal of Rock Mechanics and Mining Sciences*, *62*, 59–67. https://doi.org/10.1016/j.ijrmms.2013.04.004

Edmond, J., & Paterson, M. (1972). *Volume changes during the deformation of rocks at high pressures*. Paper presented at the International Journal of Rock Mechanics and Mining Sciences & Geomechanics Abstracts.

Goodfellow, S. D., & Young, R. P. (2014). A laboratory acoustic emission experiment under in situ conditions. *Geophysical Research Letters*, *41*, 3422–3430. https://doi.org/10.1002/2014GL059965

Graham, C. C., Stanchits, S., Main, I. G., & Dresen, G. (2010). Comparison of polarity and moment tensor inversion methods for source analysis of acoustic emission data. *International Journal of Rock Mechanics and Mining Sciences*, *47*(1), 161–169. https://doi.org/10.1016/j.ijrmms.2009.05.002

Hoek, E., & Martin, C. D. (2014). Fracture initiation and propagation in intact rock—A review. *Journal of Rock Mechanics and Geotechnical Engineering*, *6*(4), 287–300. https://doi.org/10.1016/j.jrmge.2014.06.001

Huang, J., Chen, G., Zhao, Y., & Wang, R. (1990). An experimental study of the strain field development prior to failure of a marble plate under compression. *Tectonophysics*, *175*(1–3), 269–284.

Ingraffea, A. R., & Heuze, F. E. (1980). Finite element models for rock fracture mechanics. *International Journal for Numerical and Analytical Methods in Geomechanics*, *4*(1), 25–43. https://doi.org/10.1002/nag.1610040103

Kwiatek, G., Goebel, T. H. W., & Dresen, G. (2014). Seismic moment tensor and b value variations over successive seismic cycles in laboratory stick-slip experiments. *Geophysical Research Letters*, *41*(16), 5838–5846. https://doi.org/10.1002/2014GL060159

Lajtai, E. (1974). Brittle fracture in compression. *International Journal of Fracture*, *10*(4), 525–536. https://doi.org/10.1007/BF00155255

Li, B. Q., & Einstein, H. H. (2017). Comparison of visual and acoustic emission observations in a four point bending experiment on Barre granite. *Rock Mechanics and Rock Engineering*, *50*(9), 2277–2296. https://doi.org/10.1007/s00603-017-1233-z

Li, Y., Chen, L., & Wang, Y. (2005). Experimental research on pre-cracked marble under compression. *International Journal of Solids and Structures*, *42*(9–10), 2505–2516. https://doi.org/10.1016/j.ijsolstr.2004.09.033

Lockner, D. A., Byerlee, J. D., Kuksenko, V., Ponomarev, A., & Sidorin, A. (1991). Quasi-static fault growth and shear fracture energy in granite. *Nature*, *350*(6313), 39–42. https://doi.org/10.1038/350039a0

McLaskey, G. C., Kilgore, B. D., Lockner, D. A., & Beeler, N. M. (2014). Laboratory generated M −6 earthquakes. *Pure and Applied Geophysics*, *171*(10), 2601–2615. https://doi.org/10.1007/s00024-013-0772-9

Moradian, Z., Einstein, H. H., & Ballivy, G. (2015). Detection of cracking levels in brittle rocks by parametric analysis of the acoustic emission signals. *Rock Mechanics and Rock Engineering*, *49*(3), 785–800. https://doi.org/10.1007/s00603-015-0775-1

Nolen-Hoeksema, R., & Gordon, R. (1987). *Optical detection of crack patterns in the opening-mode fracture of marble*. Paper presented at the International Journal of Rock Mechanics and Mining Sciences & Geomechanics Abstracts.

Ohno, K., & Ohtsu, M. (2010). Crack classification in concrete based on acoustic emission. *Construction and Building Materials*, *24*(12), 2339–2346. https://doi.org/10.1016/j.conbuildmat.2010.05.004

Ohtsu, M. (1991). Simplified moment tensor analysis and unified decomposition of acoustic emission source: Application to in situ hydro-fracturing test. *Journal of Geophysical Research*, *96*(B4), 6211–6221. https://doi.org/10.1029/90JB02689

Ohtsu, M. (1995). Acoustic-emission theory for moment tensor analysis. *Research in Nondestructive Evaluation*, *6*(3), 169–184. https://doi.org/10.1080/09349849508968097

Ohtsu, M., Isoda, T., & Tomoda, Y. (2007). Acoustic emission techniques standardized for concrete structures. *Journal of Acoustic Emission*, *25*(2007), 21–32.

Petit, J. P., & Barquins, M. (1988). Can natural faults propagate under mode II conditions? *Tectonics*, *7*(6), 1243–1256. https://doi.org/10.1029/TC007i006p01243

Physical Acoustic Corporation (2001). *AEwinTM SOFTWARE installation, operation and user's reference manual, SAMOS AE SYSTEM USER'S MANUAL. MISTRAS Group, Inc., Products&Systems Division* New Jersey: Princeton Junction.

Physical Acoustic Corporation (2011a). Model Nano30. Retrieved from http://www.physicalacoustics.com/content/literature/sensors/Model_Nano30.pdf

Physical Acoustic Corporation (2011b). Model PICO. Retrieved from http://www.physicalacoustics.com/content/literature/sensors/Model_PICO.pdf

Ramez, M. R. H., & Murrell, S. A. F. (1964). A petrofabric analysis of Carrara marble. *International Journal of Rock Mechanics and Mining Sciences*, *1*(2), 217–229. https://doi.org/10.1016/0148-9062(64)90028-2

Stanchits, S., Fortin, J., Gueguen, Y., & Dresen, G. (2009). Initiation and propagation of compaction bands in dry and wet Bentheim sandstone. *Pure and Applied Geophysics*, *166*(5–7), 843–868. https://doi.org/10.1007/s00024-009-0478-1

Thompson, B. D., Young, R. P., & Lockner, D. A. (2009). Premonitory acoustic emissions and stick-slip in natural and smooth-faulted westerly granite. *Journal of Geophysical Research*, *114*, B02205. https://doi.org/10.1029/2008JB005753

Tsai, S.-T., Chang, C.-D., Chang, C.-H., Tsai, M.-X., Hsu, N.-J., & Hong, T.-M. (2015). Power-law ansatz in complex systems: Excessive loss of information. *Physical Review E*, *92*(6), 062925. https://doi.org/10.1103/PhysRevE.92.062925

Wong, L. N. Y., & Einstein, H. H. (2009a). Systematic evaluation of cracking behavior in specimens containing single flaws under uniaxial compression. *International Journal of Rock Mechanics and Mining Sciences*, *46*(2), 239–249. https://doi.org/10.1016/j.ijrmms.2008.03.006

Wong, L. N. Y., & Einstein, H. H. (2009b). Crack coalescence in molded gypsum and Carrara marble: Part 2—Microscopic observations and interpretation. *Rock Mechanics and Rock Engineering*, *42*(3), 513–545. https://doi.org/10.1007/s00603-008-0003-3

Xiong, Q., & Wong, L. (2017). *Comparison of three source types for calibrating AE sensors used in fracture coalescence tests*. Paper presented at the 51st US Rock Mechanics/Geomechanics Symposium, San Francisco, CA.

Zang, A., Wagner, F., Stanchits, S., Dresen, G., Andresen, R., & Haidekker, M. (1998). Source analysis of acoustic emissions in Aue granite cores under symmetric and asymmetric compressive loads. *Geophysical Journal International*, *135*(3), 1113–1130. https://doi.org/10.1046/j.1365-246X.1998.00706.x

Zang, A., Wagner, F., Stanchits, S., Janssen, C., & Dresen, G. (2000). Fracture process zone in granite. *Journal of Geophysical Research*, *105*(B10), 23,651–23,661. https://doi.org/10.1029/2000JB900239

Zhao, Y.-H., Huang, J.-F., & Wang, R. (1993). *Real-time SEM observations of the microfracturing process in rock during a compression test*. Paper presented at the International journal of rock mechanics and mining sciences & geomechanics abstracts.

Zhu, L., & Ben-Zion, Y. (2013). Parametrization of general seismic potency and moment tensors for source inversion of seismic waveform data. *Geophysical Journal International*, *194*(2), 839–843. https://doi.org/10.1093/gji/ggt137

Zietlow, W. K., & Labuz, J. F. (1998). Measurement of the intrinsic process zone in rock using acoustic emission. *International Journal of Rock Mechanics and Mining Sciences*, *35*(3), 291–299. https://doi.org/10.1016/S0148-9062(97)00323-9